PUBLICATIONS OF THE ASTRONOMICAL SOCIETY OF THE PACIFIC, **122**:162–200, 2010 February

Imaging Young Giant Planets From Ground and Space

CHARLES A. BEICHMAN

NASA Exoplanet Science Institute, Jet Propulsion Laboratory, California Institute of Technology, Pasadena, CA 91125

JOHN KRIST AND JOHN T. TRAUGER

NASA Exoplanet Science Institute, Jet Propulsion Laboratory, California Institute of Technology, Pasadena, CA 91125

TOM GREENE

NASA Ames Research Center, Mountain View, CA 94035

BEN OPPENHEIMER AND ANAND SIVARAMAKRISHNAN

American Museum of Natural History, New York, NY 10024

RENÉ DOYON

Université de Montréal, Montréal, Quebec, H3C 3J7 Canada

ANTHONY BOCCALETTI

Observatoire de Paris, Université Pierre et Marie Curie, 92195 Meudon, France

TRAVIS S. BARMAN

Lowell Observatory, Flagstaff, AZ 86001

AND

MARCIA RIEKE

Steward Observatory, University of Arizona, Tucson, AZ 85721

Received 2009 August 31; accepted 2009 December 28; published 2010 February 5

ABSTRACT. High-contrast imaging can find and characterize gas giant planets around nearby young stars and the closest M stars, complementing radial velocity and astrometric searches by exploring orbital separations inaccessible to indirect methods. Ground-based coronagraphs are already probing within 25 AU of nearby young stars to find objects as small as ~3 $M_{\rm Jup}$. This paper contrasts near-term and future ground-based capabilities with high-contrast imaging modes of the *James Webb Space Telescope* (*JWST*). Monte Carlo modeling reveals that *JWST* can detect planets with masses as small as $0.2\ M_{\rm Jup}$ across a broad range of orbital separations. We present new calculations for planet brightness as a function of mass and age for specific *JWST* filters and extending to $0.1\ M_{\rm Jup}$.

1. INTRODUCTION

As coronagraphic and adaptive optics (AO) technologies improve, the number of directly imaged planets is increasing, most recently with four companions being detected in orbit around two nearby A stars. Because the three planets around HR8799 (Marois et al. 2008) and the single planet around Fomalhaut (Kalas et al. 2008) are young, their internal reservoirs of gravitational energy generate enough luminosity to make these objects visible (Saumon et al. 1996). In addition, there is an as-yet-unconfirmed planet seen once around β Pic (Lagrange et al. 2009). These young planets plus earlier discoveries, e.g., 2M1207-3932b (Chauvin et al. 2005) and GQ Lup b (Neuhäuser et al. 2005), are confirmed to be companions via their common proper motion with their host star and in a number of cases by orbital motion as well. While it is possible to use estimated ages and evolutionary tracks to distinguish in a gross sense between planets ($<13\ M_{\rm Jup}$, the deuterium burning limit), brown dwarfs ($13 < M < 70\ M_{\rm Jup}$, the hydrogen-burning limit) and low-mass stars ($>70\ M_{\rm Jup}$), it is difficult to assign a reliable mass to directly imaged companions. In some cases, dynamical estimates based on the configuration of the debris disk constrain the planet mass, e.g., $<3\ M_{\rm Jup}$ for Fomalhaut b (Kalas et al. 2008; Chiang et al. 2009).

The relationships between near-IR brightness, age, and mass are uncertain, and dynamical mass determinations are difficult for planets on long period orbits, particularly in the absence of a dust disk. What is needed to anchor the models of young planets are objects of known age with a combination of imaging (giving luminosity and effective temperature) plus dynamical information (giving mass). This combined information will come from direct imaging and dynamical mass measurements from ground-based radial velocity (RV) or astrometry from either the ground (Van Belle et al. 2008; Pott et al. 2008) or space using the *Space Interferometry Mission* Lite (*SIM* Lite, Beichman 2001; Tanner et al. 2007) or GAIA (Sozzetti et al. 2008). Detections of transiting young planets would be extremely valuable, but the variability of young host stars may make these planets hard to detect, and the extreme environment of "hot Jupiters" may make it difficult to draw general conclusions.

Direct imaging has opened a new region of the mass-semimajor axis (SMA) parameter space for planets (Fig. 1) and has given rise to new theoretical challenges. The existence of giant planets at separations larger than ~10 AU is difficult to account for in standard core-accretion models (Pollack et al. 1996; Ida & Lin 2005; Dodson-Robinson et al. 2009) and a different formation mechanism, gravitational fragmentation in the disk (Boss 2000), may be operating. Alternatively, a combination of the two mechanisms may be responsible for these distant planets, with outward migration or planet-planet scattering

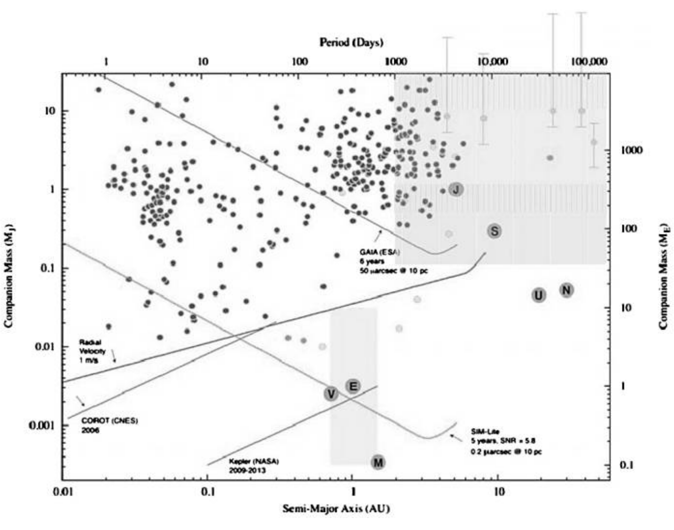

FIG. 1.—Distribution of detected planets (as of mid-2009 as taken from the Exoplanet Encyclopedia, Schneider 2009) in the mass-semimajor axis (SMA) plane. Different techniques dominate in different parts of this parameter space: transits in the upper left corner (*circles*); radial velocity detections between 0.01–5 AU and above 0.01 $M_{\rm Jup}$ (*circles*); direct imaging detections in the upper right hand corner (*error bars*); a few microlensing detections (*circles*) between 1–5 AU; and three pulsar timing planets (*points*). Sensitivity limits for various techniques are shown as *solid lines* (RV, transit, and astrometry). The top shaded area in the upper right shows the region that will be probed by ground-based imaging in the coming decade (*upper,* $>1\ M_{\rm Jup}$) and by *JWST* (*lower,* $<1\ M_{\rm Jup}$). Figure courtesy of Peter Lawson (JPL). See the electronic edition of the *PASP* for a color version of this figure.

moving planets formed in dense inner regions onto orbits as distant as 100 AU (Veras et al. 2009).

There have been a number of investigations of coronagraphic imaging of planets, particularly in the context of designs for the *Terrestrial Planet Finder-Coronagraph* (*TPF-C*), including Agol (2007), Beckwith (2009), and Brown (2009). These authors have investigated the challenging task of finding planets, both gas or ice giants and terrestrial planets, through their *reflected light*. The reflected light signal depends on the inverse square of the star-planet separation, the planetary albedo, and orbital phase function with resulting planet-star contrast ratios as small as 10^{-8} to 10^{-11} (Jupiters and Earths at 1 AU, respectively). The goal of these authors has been to either optimize the design of *TPF* in terms of aperture size (Beckwith 2009) or to optimize search strategies for various TPF designs (Agol 2007). This paper addresses a more near-term and far less challenging problem, namely the detection of *self-luminous* gas giants using telescopes and instruments that either are or will become operational in the next 5–10 yr. The contrast ratios for self-luminous giant planets are far more favorable, 10^{-6} to 10^{-8}, and the details of the calculations are very different from the reflected light case.

In particular, we explore the prospects for imaging self-luminous giant planets from the ground and from space using the *JWST* (Gardner et al 2006). This application of *JWST* for exoplanet research complements recent studies (Greene et al. 2007; Deming et al. 2009) discussing its role for transit spectroscopy. We investigate how imaging surveys might yield statistical information on the distribution of planets as functions of mass and orbital location. In what follows we describe two samples of stars suitable for direct searches, nearby young stars and nearby M stars (§ 2); introduce a number of instruments suitable for planet surveys (§ 3); describe a plausible population of exoplanets (§ 4); and utilize a Monte Carlo simulation to predict the yield of surveys under different scenarios (§ 5). We explicitly examine the prospects for finding planets for which both imaging and dynamical observations might become available (§ 6).

2. THE STELLAR SAMPLE

The two most important factors from an observational standpoint in searching for planets are star-planet contrast ratio and angular resolution. Young gas giant planets generate enough luminosity via gravitational contraction to be bright in the near-IR (Saumon et al. 1996; Burrows et al. 2003), making ages less than ~1 Gyr an important characteristic of appropriate target stars. Because the inner working angles (IWA)[1] of typical observing systems are limited to a few tenths of an arcsecond (§ 3) or a few tens of AU at the distance of typical young stars, proximity of target stars is another important criterion. These astrophysical

[1]The term "inner working angle" is used to describe the off-axis angle (radius) at which the transmission of the occulting mask drops below 50%.

and observational factors, youth and proximity, lead to two natural populations for study: the closest stars with ages less than 1 Gyr, and the closest M stars for which a Jupiter-mass planet of even a few Gyr would be detectable and for which the inner few AU become accessible. The samples of stars discussed here are meant to be representative enough to allow the detectability of planets to be investigated as a function of distance and age, the two most critical variables for all imaging investigations, for a wide variety of instruments. Samples developed for individual projects will have be made more rigorously in terms of age, mass, metallicity, distance, binarity, cluster environment, etc. as appropriate to a specific set of scientific goals. For example, for simplicity in the present study we exclude binary stars despite the obvious interest in the question of planets in such systems. For close binaries, it is beyond the scope of this article to calculate properly the coronagraphic response interior to the IWA at the 10^{-7} level relevant to some of the instruments. For more widely separated binaries, the presence of an unobscured bright companion in the camera field of view (2″–15″) can wreak havoc with instrument performance. The results presented here represent lower limits to the performance on binaries.

2.1. A Sample of Young Stars

Extremely young objects, 1–5 Myr old, are found in well-known star-forming clusters associated with nearby molecular clouds such as Taurus and Chameleon (Table 1). The closest of these associations are 100–140 pc away, so that a classical coronagraph on a 5–8 m telescope could probe only beyond 15–25 AU at 1.6 μm (80 AU at 4.4 μm). An improved view of the inner parts of young planetary systems requires closer stars (or eventually a larger telescope like the proposed 30–40 m facilities). We have supplemented the youngest stars with "adolescent" stars having ages between 10 and 1 Gyr. These have been identified via X-ray emission, isochronal analysis, and common proper motion and can be as close to the Sun as 25 pc (Zuckerman & Song 2004). Depending on the wavelength and instrument, these systems can be probed to within 5–10 AU of their host stars.

We have utilized a number of compilations of infant and adolescent stars to assemble a target sample. First, ~200 stars chosen for an astrometric survey for gas giants with *SIM* Lite (Beichman 2001; Tanner et al. 2007) encompass both classical and weak-lined T Tauri stars with masses from 0.2–2 $M_\odot$, ages from 1 Myr up to 100 Myr, and distances from 25–140 pc. Second, the *Spitzer* FEPS survey (Meyer et al. 2006) includes over 300 stars of F, G, K spectral types with ages of roughly 10 Myr to 1 Gyr (Hillenbrand et al. 2008). Third, a group of A stars selected for debris disk observations with *Spitzer* (Rieke et al. 2005) includes clusters out to several hundred pc. We restricted the A-star sample to 150 pc and added additional single A0–A9 (IV/V or V) stars with credible ages to obtain a more complete sample of almost 200 stars out to 50 pc. The properties of the various samples are given in Tables 1 and 2 and illustrated in Figures 2 and 3.

2.1.1. Influence of Stellar Properties on Incidence of Planets

Various stellar properties may affect the likelihood of a star developing and retaining a planetary system, including stellar mass, metallicity, and the presence of disks.

High stellar mass may enhance the probability of a star having one or more gas giant planets. There are theoretical grounds for expecting this effect (Ida & Lin 2005; Dodson-Robinson et al. 2009) as well as observational hints from observations of subgiants with 1–2 $M_\odot$ precursors. Johnson (2007) shows a factor of 3 increase in the incidence of RV-detected planets between host stars with 0.5–1.5 $M_\odot$ and those with masses $>1.5\ M_\odot$. Conversely, low-mass M stars appear to have a smaller incidence of gas giant planets as determined from RV studies (Butler et al. 2006) and initial coronagraphic surveys (McCarthy & Zuckerman 2001; Oppenheimer et al. 2001; Oppenheimer & Hinckley 2009; Metchev & Hillenbrand 2009). We have taken these effects into account in our modeling (§ 4) by (a) increasing the incidence of higher-mass planets around stars with mass greater than 1.5 $M_\odot$, and (b) restricting the incidence of high-mass planets around low-mass stars. It is well known that

TABLE 1
PROPERTIES OF NEARBY CLUSTERS

Cluster	Age (Myr)	Distance (pc)	Cluster	Age (Myr)	Distance (pc)
β Pic (T08, ZS04)	10–12	31 ± 21	Pleiades (P04, M01)	120	135 ± 2
Tucanae-Horologium (T08, ZS04)	30	48 ± 7	Chamaeleon (T08)	6	108 ± 9
Taurus-Aurigae (E78)	Range ~1–10	140 ± 10			
TW Hya (T08, ZS04)	8	48 ± 13	Upper Sco, Sco Cen (W08, PZ99)	2–5	130 ± 10

NOTE.—Characteristic distances to clusters can be misleading since clusters may have considerable depth along the line sight. Ages are derived with respect to pre–main-sequence evolutionary tracks (e.g., Siess et al. 2000), lithium abundances, and kinematics, and their absolute accuracy is probably no better than a factor of 2%, particularly for extremely young objects. However, our knowledge of the relative ages of various clusters is considerably better.

REFERENCES.—(T08) Torres et al. 2008; (ZS04) Zuckerman & Song 2004; (P04) Pan et al. 2004; (M01) Martin et al. 2001; (W08) Wilking et al. 2008; (E78) Elias 1978; (PZ99) Preibisch & Zinnecker 1999.

TABLE 2

NUMBERS OF STARS IN STELLAR SAMPLES

SIM Lite Young Star Project	217
Spitzer FEPS Project	306
Spitzer plus nearby A stars	188
Nearby M stars (<15 pc)	196

higher metallicity enhances the probability of mature stars to have Jupiter-mass giant planets (Valenti & Fischer 2005), but results for planets of lower mass suggest that this effect is not important for Neptune-mass planets (Sousa et al. 2009). Almost nothing is known about whether or how these effects operate at the larger orbital distances probed by imaging surveys. Although Agol (2007) shows that biasing a survey to high metallicity can improve a survey's yield by 14%–19%, we do not include this effect in the models considered herein. If one simply wants to maximize the probability of finding (high-mass) planets, then one might take these trends into account by focusing on high-mass, high-metallicity stars. However, understanding these dependencies (particularly if the population of distant planets differs from interior planets) must be addressed via unbiased surveys.

Debris or protostellar disks can present a challenge for planet searches. They may serve as marker for the presence of planets, e.g., Fomalhaut and possibly β Pic, but may also mask the presence of planets if the diffuse emission is bright enough. For most of the coronagraphic targets considered here, we show that the search for self-luminous planets is unaffected by diffuse emission.

Target Selection. We excluded target stars with large amounts of nebulosity and/or optically thick disks, i.e., high values of disk to stellar luminosity (L_d/L_*). This restriction excludes obscured or partially obscured objects which are typically the youngest protostars still possessing primordial, gas-rich disks. For example, the detection of planets of even Jovian mass would be extremely difficult within the disk of AB Aur, which has a disk with $L_d/L_* \sim 0.6$ (Tannirkulam et al. 2008). The *SIM* Lite sample was explicitly chosen to exclude objects with nebulosity by inspection of imaging data (Tanner et al. 2007). The *Spitzer* data for the FEPS sample revealed only six objects with high optical depth disks, i.e., $L_d/L_* > 0.01$ (Hillenbrand et al. 2008). The other 26 sources in the FEPS sample with prominent *Spitzer* disks had an average value of log $(L_d/L_*) = -3.8$ with a dispersion of ± 0.5, comparable to the range bounded by β Pic and Fomalhaut.

Residual Diffuse Emission. We developed a very simple model of diffuse emission appropriate to the stars and spatial

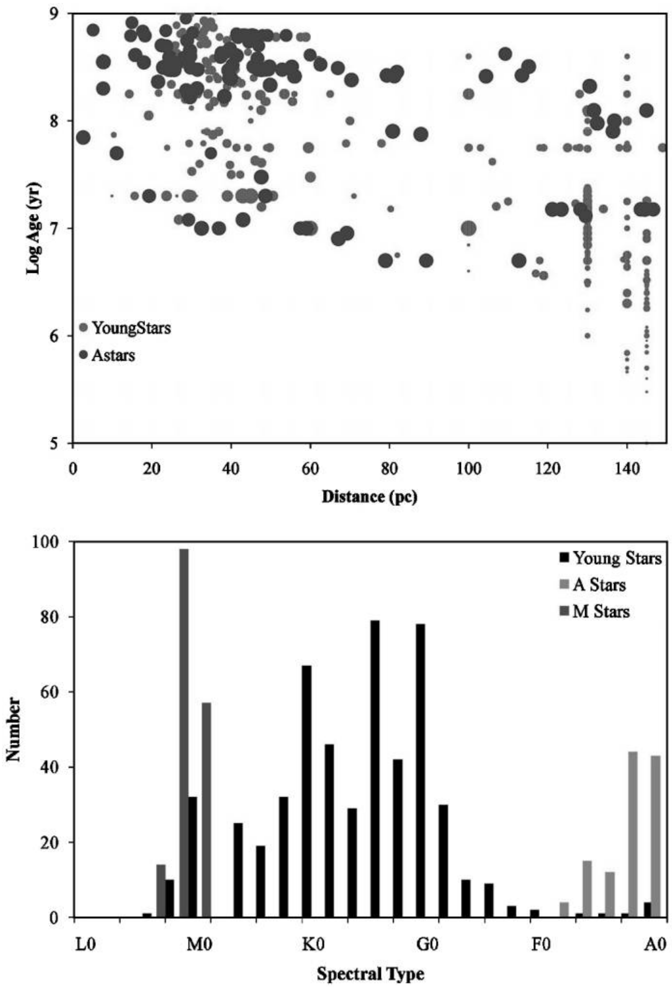

FIG. 2.—(*Top*) Sample of young A, F, G, K, and M stars covers a range of ages from under 1 Myr up to 1 Gyr and distances from 5 to 150 pc. The size of the circle denotes spectral type from A stars (largest) to M stars (smallest). (*Bottom*) The distribution of spectral types among the SIM + FEPS and A star samples (which together comprise the "young star" sample) and M star sample. See the electronic edition of the *PASP* for a color version of this figure.

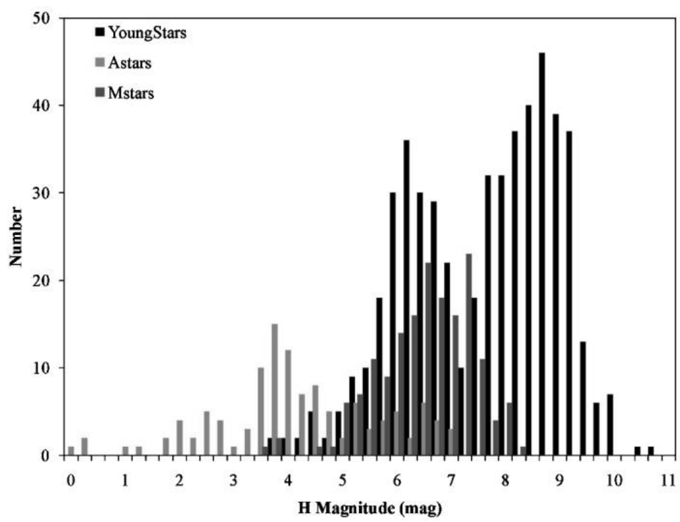

FIG. 3.—Stars in the various samples cover a broad range of H magnitudes, which can be an important parameter when considering the performance of adaptive optics systems. See the electronic edition of the *PASP* for a color version of this figure.

scales examined in these simulations (~5–100 AU) and then calculated the flux density of spurious point sources relative to the brightness of the star. As will be discussed, the level of spurious objects due to clumps in the local background is well below the level of residual scattered starlight in the instruments considered here for self-luminous planets and typical disks, i.e., $\log(L_d/L_*) = -3.8$.

Finally, it is well known that stellar ages are difficult to estimate. We investigated this effect on the simulations by allowing the age to vary with a log-normal distribution having a dispersion of a factor of 2 around the nominal age. The average properties of the detected planets were not appreciably affected by this variation. Younger ages made some planets more easily detectable, while older planets fell below detection limits. The derived properties, especially the mass, of a planet detected around any particular star will depend, of course, on the uncertain age of the parent star.

2.2. A Sample of Nearby M Stars

The very closest stars to the Sun also offer the prospect of finding self-luminous planets. Nearby M stars are advantageous since the parent star is 5–10 mag fainter than higher-mass stars, leading to a more favorable contrast ratio for self-luminous planets, and because their proximity to the Sun can expose planets located within a few AU of the star. Unfortunately, field M stars are typically older than 1 Gyr, implying that their planets will be faint. Further, these visually faint stars are relatively poor targets for ground-based adaptive optics systems relying on visible stellar photons for wavefront correction. Nevertheless, a dozen objects of potentially planetary mass have been found around M stars either via RV (GJ 876b) or imaging (*Two Micron All Sky Survey,* 2MASS 1207b), so it is useful to consider what objects might be detectable with imaging. We have assembled a list of 196 M stars (M0-M9V) within 15 pc that either are single or whose companions are at least 30″ distant, according to the SIMBAD and NStED databases. We added to the sample AU Mic (GJ 803) and AT Mic which, although they are in multiple systems, are young and therefore potential hosts of bright planets. The AU Mic debris disk (Plavchan et al. 2009) has a disk-to-star luminosity ratio of $\log(L_d/L_*) = -3.4$, which is not enough to impede detection of most planets (§ 3.3). We derived very approximate ages for the stars using their X-ray luminosity (when available) and a X-ray–age relationship derived from Preibisch & Feigelson (2005; their Fig. 4). For the 100 nearby M stars in our sample without this information, we adopted a representative age of 5 Gyr (Zapatero Osorio et al. 2007).

3. THE INSTRUMENTS

The key parameters of an instrument used for direct imaging of planets are its inner and outer working angles (OWA), its starlight rejection as a function of angular separation from a target star, and its optical efficiency and sensitivity. We discuss these parameters for a number of ground-based and space-based instruments. For ground-based instruments we include the currently operational Near-Infrared Infrared Coronagraph (NICI) on the Gemini Telescope (Biller et al. 2009), which is comparable in performance to the Subaru/HiCIAO instrument (Suzuki et al. 2009), as well as next-generation coronagraphs in development for the Palomar telescope (P1640), the Gemini Planet Imager and SPHERE on the VLT, and an idealized coronagraph on a 30 m telescope (TMT). We include a ground-based 5 μm capability based on the Multiple Mirror Telescope (MMT). These ground-based capabilities are contrasted with three *JWST* instruments: a Lyot coronagraph on NIRCam (various wavelengths from 2.1–4.6 μm), a nonredundant mask on the Tunable Filter Instrument (TFI/NRM), and a four-quadrant phase mask on the Mid-Infrared Instrument (MIRI/FQPM). This information is summarized in Tables 3 and 4 and Figure 4a.

The IWA of a telescope of diameter, D, equipped with a Lyot coronagraph has a typical radial extent of ~$2 - 5\lambda/D$, or typically a few tenths of an arcsec in the near-IR. For a classical Lyot coronagraph, the IWA is defined unambiguously by a hard-edged mask, while for a band-limited coronagraph, the IWA is not a single number but can be defined as the angle at which the off-axis transmission drops below 50%. The OWA of an instrument depends on such parameters as the size of the detector array in a simple imaging coronagraph, the number of actuators in a deformable mirror, or the size of a subaperture in an interferometric system. Table 3 summarizes this information and projects this angular scale out to different distances. It is clear from the table that probing the region interior to 100 AU requires target systems within 150 pc and preferably much closer.

3.1. Ground-based Coronagraphs

Coronagraphs on large ground-based telescopes are evolving rapidly with advances in coronagraph design, extreme adaptive optics, and postcoronagraph wavefront control. The current generation of coronagraphs are finding young gas giants, e.g., HR 8799, and new instruments such as Subaru/HiCIAO and Gemini/NICI will push these searches to lower masses and smaller orbits with contrast ratios of $\Delta\mathrm{Mag} = 13 - 15$ mag (Biller et al. 2009; Wahhaj et al. 2009). The next-generation instruments, including P1640 at Palomar Mountain (Hinkley et al. 2008; Sivaramakrishnan et al. 2009), the Gemini Planet Imager (GPI) (Macintosh et al. 2006) and the SPHERE instrument (Beuzit et al. 2006; Boccaletti et al. 2008) on the Very Large Telescope (VLT), will achieve contrast ratios of $\Delta\mathrm{Mag} \sim 18$ mag at 1″ and thus probe masses ~ few M_{Jup}. P1640 will be limited to northern hemisphere targets whereas many of the nearest, young stars are visible only from southern observatories. GPI and SPHERE with observe southern targets with contrast limits comparable to P1640's but with improved angular resolution and magnitude limits due to their larger apertures. We project the performance

TABLE 3
INNER WORKING ANGLE AND PHYSICAL RESOLUTION

Telescope (m)	5.0	6.5	6.5	6.5	8.0	30.0
Wavelength (μm)	1.65	2.2	4.4	11.4	1.65	1.65
Inner Working Angle (mas)						
NIRCAM/Wedge ($4\lambda/D$)	—	280	560	—	—	—
NIRCAM/Sombrero ($6\lambda/D$)	—	420	850	—	—	—
"MMT-like" ($4\lambda/D$)	—	—	560	—	—	—
TFI/Nonredundant Mask ($0.5\lambda/D$)	—	35	70	—	—	—
MIRI/FPQM ($1\lambda/D$)	—	—	—	365	—	—
Palomar/P1640 ($2.5\lambda/D$)	170	—	—	—	—	—
GPI/SPHERE ($2.5\lambda/D$)	—	—	—	—	105	—
TMT Coronagraph ($2.5\lambda/D$)	—	—	—	—	—	30
Physical Resolution (AU) at 10 pc						
NIRCAM/Wedge ($4\lambda/D$)	—	2.8	5.6	—	—	—
NIRCAM/Sombrero ($6\lambda/D$)	—	4.2	8.5	—	—	—
"MMT-like"($4\lambda/D$)	—	—	5.6	—	—	—
TFI/Nonredundant Mask ($0.5\lambda/D$)	—	0.4	0.7	—	—	—
MIRI/FPQM ($1\lambda/D$)	—	—	—	3.7	—	—
Palomar/P1640 ($2.5\lambda/D$)	1.7	—	—	—	—	—
GPI/SPHERE ($2.5\lambda/D$)	—	—	—	—	1.1	—
TMT Coronagraph ($2.5\lambda/D$)	—	—	—	—	—	0.3
Physical Resolution (AU) at 50 pc						
NIRCAM/Wedge ($4\lambda/D$)	—	14	28	—	—	—
NIRCAM/Sombrero ($6\lambda/D$)	—	21	42	—	—	—
"MMT-like" ($4\lambda/D$)	—	—	28	—	—	—
TFI/Nonredundant Mask ($0.5\lambda/D$)	—	1.8	3.7	—	—	—
MIRI/FPQM ($1\lambda/D$)	—	—	—	18	—	—
Palomar/P1640 ($2.5\lambda/D$)	9	—	—	—	—	—
GPI/SPHERE ($2.5\lambda/D$)	—	—	—	—	5	—
TMT Coronagraph ($2.5\lambda/D$)	—	—	—	—	—	1.5
Physical Resolution (AU) at 140 pc						
NIRCAM/Wedge ($4\lambda/D$)	—	40	80	—	—	—
NIRCAM/Sombrero ($6\lambda/D$)	—	60	120	—	—	—
"MMT-like" ($4\lambda/D$)	—	—	80	—	—	—
TFI/Nonredundant Mask ($0.5\lambda/D$)	—	5	10	—	—	—
MIRI/FPQM ($1\lambda/D$)	—	—	—	50	—	—
Palomar/P1640 ($2.5\lambda/D$)	24	—	—	—	—	—
GPI/SPHERE ($2.5\lambda/D$)	—	—	—	—	15	—
TMT Coronagraph ($2.5\lambda/D$)	—	—	—	—	—	4

of future coronagraphs on the next generation of $30+$ m telescopes such as the TMT, GMT, and E-ELT, adopting a contrast ratio floor of 10^{-8} in the midrange of what has been discussed for these highly segmented telescopes (Macintosh et al. 2006). It is important to note that ground-based coronagraphs operating with extreme adaptive optics systems require bright target stars for the extreme wavefront control needed for contrast ratios of $\ll 10^{-6}$. Stars fainter than $R \sim 8$ mag ($H \sim 5$–7 mag for typical FGKM stellar colors) will have poorer coronagraphic performance (Fig. 3).

Finally, we note that ground-based imaging searches at 3 and 5 μm are already underway, trading increased planet brightness against higher thermal backgrounds (Heinze et al. 2008; Kenworthy et al. 2009). With L′ and M-band sensitivities of ∼16 mag and 14 mag (5σ), respectively, on the MMT (Heinze et al. 2008), surveys with instruments like Clio should be able to probe the 5–10 $M_{\rm Jup}$ range within 10–100 AU. In the longer term, interferometry with the Large Binocular Telescope Interferometer (LBTI) offers the prospect of examining nearby young stars with <50 mas resolution. However, the 8–10 magnitudes of difference in sensitivity between *JWST* (Table 4) and ground-based telescopes will gave *JWST* a substantial advantage for the imaging surveys considered here. We approximate the performance of a ground-based 5 μm coronagraph on a large telescope by adopting the characteristics of NIRCam's coronagraph but with a magnitude floor of $M = 14$ mag.

TABLE 4
ILLUSTRATIVE PROPERTIES OF CORONAGRAPHS USED IN SIMULATIONS

Instrument	Wavelength (μm)	ΔMag[a] at θ 0.5″	1″	2″	4″	Sens. Limit[b] (5σ, 1 hr mag)
NICI	1.65 μm	12	14	14.5		20
P1640	1.65 μm	16	18	18	18	20
GPI	1.65 μm	17.5	18	18	18	21
"MMT-like"	4.3 μm	9.9	11.7	14.3	16.2	14
TMT	1.65 μm	17.5	17.5	17.5	17.5	22.5
NIRCam Spot	3.35 μm	9.9	12.4	15.1	17.8	24.8
NIRCam Spot	4.4 μm	9.9	11.7	14.3	16.2	23.6
TFI/NRM w. Cal.	4.70 μm	12.5	—	—	—	20.6
TFI/NRM w/o Cal.	4.70 μm	10.0	—	—	—	20.6
MIRI/4QPM	11.4 μm	9.0	9.5	12	13	17.6

[a] Rejection ratios are 5σ See test for references for individual instruments.
[b] Sensitivity limits are 5σ in the difference of two 3600 s exposures and include a degradation for lower coronagraphic throughput.

3.2. High-Contrast Imaging with the *James Webb Space Telescope* (*JWST*)

Three of the instruments on *JWST* have capabilities for high-contrast imaging. We present performance information on the coronagraphs planned for the Near-IR camera (NIRCam), the Tunable Filter Instrument (TFI), and the Mid-Infrared Instrument (MIRI). The calculations of contrast performance combine diffraction-based estimates of telescope performance including 131 nm of total wavefront error (Stahl 2007) with instrument performance models provided by the instrument team members (coauthors on this article) responsible for those modes. The reader is referred to the references quoted in each section for details. Since the *JWST* mirror is still being fabricated, estimates of telescope performance are subject to change. While the wavefront error is relatively large compared to standards of advanced AO systems (50 nm) or future coronagraphs designed to search for earths (1 nm for TPF-C; Trauger and Traub 2007), *JWST* will operate under extremely stable conditions (perhaps 10–20 nm variations over a few hours) and with extremely low backgrounds in the near- and mid-infrared where young exoplanets are bright. *JWST* achieves its (modest) imaging quality without reference to a bright target star, making it well suited to searching for planets around faint stars inaccessible to ground-based telescopes.

We do not examine the performance of *JWST* at wavelengths $\leq 2\ \mu$m for two reasons. First, *JWST*'s coronagraphic performance at short wavelengths will depend critically on the (as yet) poorly known wavefront errors of the mirror, making such predictions premature. Second, at short wavelengths, 8–30 m ground-based telescopes with extreme AO will have significant advantages over *JWST* for bright stars in imaging situations where scattered starlight dominates the noise and where large collecting areas can overcome modest sky backgrounds.

3.2.1. NIRCam

The NIRCam instrument (Rieke et al. 2005) includes a coronagraph with five focal plane masks (Fig. 5). Three round spots or "Sombrero"-shaped masks and two wedge-shaped masks are optimized for design wavelengths of 2.1, 3.35, 4.3, and 4.6 μm (Table 4; Green et al. 2005; Krist et al. 2007). The occulting spots are apodized, but only quasi-band limited (Kuchner & Traub 2002) since the wavefront error in the *JWST* telescope is sufficiently large that the coronagraphic performance is dominated by the telescope scattering not by diffraction. The performance of the five masks is predicted on the basis of a full diffraction calculation assuming nominal performance of the segmented *JWST* primary and using appropriate Lyot stops and occulting spots (Krist 2007). Figure 6 shows contrast ratios after speckle suppression has been carried out using roll subtraction (± 5 deg is allowed during *JWST* operations) and assuming a random position offset error of 10 mas between rolls and random wavefront variations of 10 nm. At 1″ from the central star, *JWST* should achieve almost 12 magnitudes of suppression while at 4″ the suppression will approach 18 mag. For the survey simulations described here we have used the predicted performance of the 4.3 μm (design wavelength) spot with an inner working angle of $6\lambda/D \sim 850$ mas. Comparable results are obtained for the 4.6 μm wedge occulter. Examination of Figure 6 suggests that the spot occulter performs better at larger separations while the wedge works better at smaller angles. As discussed in § 3.2.2, this expectation is confirmed in the simulations, although the differences are small. We examine NIRCam performance in two filters, F444W and F356W, using sensitivity limits appropriate to the difference of two 1 hr exposures (Rieke et al 2005[2]), degraded by a factor of 2 for the

[2] At http://ircamera.as.arizona.edu/nircam/features.html.

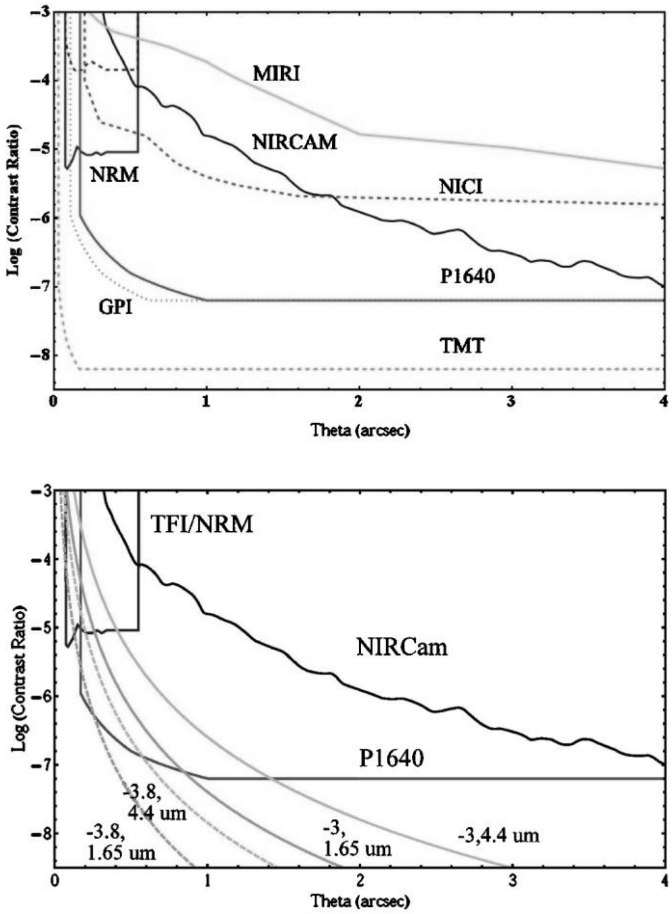

FIG. 4.—(*Top*) Performance (5σ) of 7 high contrast imaging systems is shown in terms of contrast ratio as a function of off-axis angle: MIRI with 4 Quadrant Phase Mask at 11.4 μm (*top curve*); NIRCam Lyot coronagraph at 4.4 μm (*black*); Gemini NICI instrument (*dashed*); P1640 at 1.65 μm with an extension to smaller inner working angles for GPI operating n an 8 m telescope (*dotted*); an idealized coronagraph on a 30 m telescope (TMT) operating at 1.65 μm (*dashed curve*). Inside of 1″ we show two curves for the nonredundant mask (NRM) at 4.4 μm with and without visibility calibration (*solid* and *dotted curves*). (*Bottom*) The NIRCam, P1640, and TFI/NRM curves are repeated along with curves showing the brightness of potential spurious sources from diffuse scattered emission associated with debris disks as observed with *JWST* at 4.4 μm and 1.65 μm with P1640. Noise from disks with $L_d/L_* = 10^{-3}$ and $10^{-3.8}$ shown as *solid* and *dashed*, respectively. The details are described in the text. See the electronic edition of the *PASP* for a color version of this figure.

lower throughput of NIRCam (20% vs. $>80\%$) with the coronagraphic pupil mask.

3.2.2. *The* JWST *Nonredundant Mask (NRM)*

The Fine Guidance System on *JWST* incorporates a near-IR science camera equipped with a tunable filter instrument (TFI; Doyon et al. 2008). In addition to standard coronagraphic imaging modes, the TFI provides an important complement to the NIRCam coronagraph. The nonredundant mask (NRM) is a true interferometer which will take advantage of *JWST*'s extreme stability to make high-contrast images at high angular resolution (Sivaramakrishnan et al. 2009). By masking out all but 7 subapertures, each with projected size of $D_s \sim 1$ m across *JWST*'s 6.5 m pupil, it is possible to create 21 independent baselines (Fig. 7) to observe with resolution $\sim 0.5\lambda/D \sim 0.07''$ over a field of view (radius) of $\sim 0.6\lambda/D_s \sim 0.55''$ (Table 3). Careful calibration of fringe visibilities with respect to reference stars should result in contrast ratios of $\Delta\mathrm{Mag} \sim 12.5$ mag (Sivaramakrishnan et al. 2009), a major improvement over typical ground-based values of 4–5 mag (Lloyd et al. 2006). If visibility calibration proves impractical, the contrast performance will be a factor of ~10 worse, i.e., $\Delta\mathrm{Mag} \sim 10$ mag. An important problem still to be addressed is the effect of detector stability on NRM performance in the presence of the unattenuated photon fluxes from bright central stars. Shot noise and possible flat-field noise due to pixel-to-pixel variations of $>10^{-5}$ will limit contrast ratios for stars with 4.4 μm magnitudes of ~5 mag or brighter.

3.2.3. *The* JWST *Mid-Infrared Imager (MIRI)*

The Mid-Infrared instrument (MIRI) on *JWST* is equipped with three four-quadrant phase masks (FQPM) operating in narrow bands ($R \sim 20$) at 10.65, 11.4, and 15.5 μm as well as with a conventional coronagraph operating at 23 μm (Rouan et al. 2007; Boccaletti et al. 2005). The latter will predominantly be used for the study of disks since its IWA will be relatively coarse ($>2.2''$). With contrast ratios in the range of $\Delta\mathrm{Mag} =$ 8–12.5 mag at an IWA (radius) of $1\lambda/D \sim 0.36''$ at 11.4 μm, the MIRI FQPM will be able to probe within 10–20 AU of the closest young host stars. The IWA for this instrument does not have a sharp edge so that companions interior to the nominal IWA would be visible but highly attenuated at $<1\lambda/D$. The MIRI/FQPM offers angular resolution between that of NIRCam and TFI/NRM, but with the advantage of a much wider field of view than TFI/NRM, up to 13″. The contrast curve shown in Figure 4 assumes subtraction of a point-spread function (PSF) reference star for speckle suppression, pointing jitter of 7 mas and a 20 nm variation in wavefront error between observations. A version of the FQPM has been in operation on the NACO instrument on the VLT since 2003 (Boccaletti et al. 2004) and the MIRI prototype has been tested in the laboratory (Baudoz et al. 2006), giving confidence that the contrast goals described here can be achieved.

3.3. Noise from Diffuse Emission

As was noted, bright nebulosity and/or a disk around a young star is a potential source of noise for planet searches. Thermal emission from dust will be negligible at the angular separations ($\gg$1 AU at 10 s of pc), stellar luminosities, and short wavelengths (<5 μm) considered here; only MIRI observations for the closest, most luminous A stars might be affected by thermal emission. We thus focus on the effects of scattered light

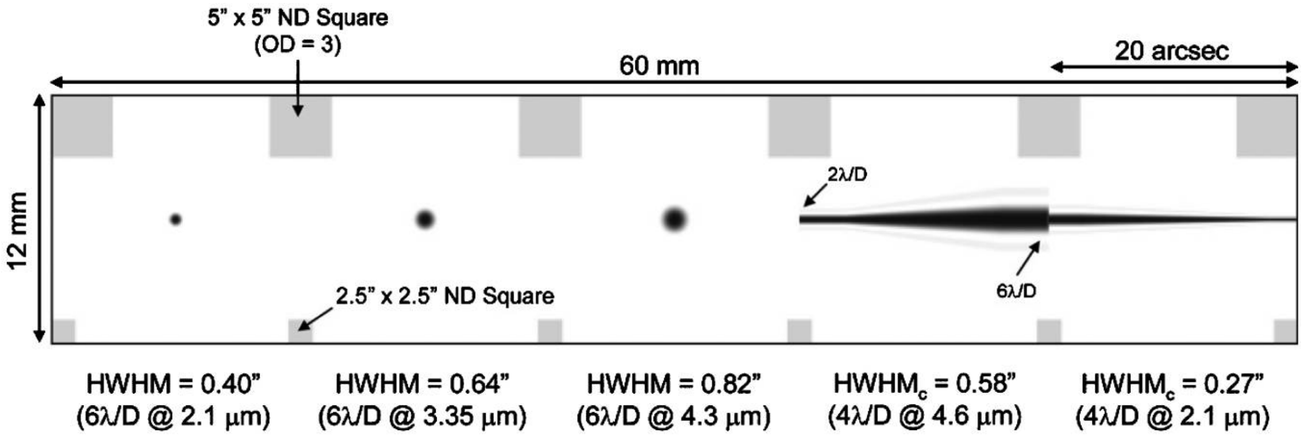

FIG. 5.—Layout of the coronagraphic focal plane masks in the NIRCam instrument includes 3 occulting spots plus 2 occulting wedges. Neutral density squares are placed across the top and bottom for source acquisition.

using observations of Fomalhaut (Kalas et al. 2008) and β Pic (Golimiski et al. 1993) to develop a simple model for the brightness of possible sources produced in clumps in diffuse scattered light at large radii. Let the radial dependence of surface brightness be modeled as $I(r) = I_0(r_0)(\frac{r}{r_0})^{-2}(\frac{r}{r_0})^{-\beta}$ where the r^{-2} term comes from the increased stellar illumination and the $r^{-\beta}$ term is due to the increasing surface density of dust as one moves closer to the star. We derived similar values of V ~ R band surface brightness of $I_0(100\ \mathrm{AU}) = 20.6$ mag arcsec^{-2} and $\beta = 2$ for Fomalhaut (face-on) to $I_0(100\ \mathrm{AU}) = 19.2$ mag arcsec^{-2} and $\beta = 1$ for β Pic (edge-on), both normalized to $L_d/L_* = 10^{-3.8}$ which is the average disk luminosity for sources in the FEPS sample (Hillenbrand et al. 2008). The brightness of a spurious point source (5σ) from a clump in the disk emission, relative to the brightness of the star, F_*, can be written $F_{\mathrm{disk}}/F_* = 5\eta I(r)\Omega/F_*$ where $\Omega \sim (\lambda/D)^2$ is the solid angle of a diffraction-limited beam and $\eta = 10\%$ is the fraction of the diffuse emission in a clump (as opposed to smooth emission, which could be subtracted out). Figure 4b includes curves based on the Fomalhaut profile for a star at 50 pc with $L_d/L_* = 10^{-3.8}$ and 10^{-3} for two instrumental cases: 1.65 μm and $D = 5$ m; and 4.4 μm and $D = 6.5$ m. The figure suggests that, *for appropriately selected stars,* spurious sources from scattered light will not be a significant problem beyond 0.5″ and only a marginal problem at smaller separations for *JWST*/NRM or ground-based telescopes. Note that we have made the conservative assumption that the scattering efficiency of the dust grains is flat rather than falling off at wavelengths >1 μm.

4. A POPULATION OF PLANETS

The combination of RV studies and transit observations has given us a good understanding of the incidence of gas and icy giant planets with masses of a few Jupiter masses down to a few tens of Earth masses located from a few stellar radii out to 5 AU (Cumming et al. 2008). Within this orbital range approximately 10%–15% of solar-type stars have gas giants ($M > 0.3\ M_{\mathrm{Jup}}$) and perhaps double that fraction if one extends the mass range to $0.01\ M_{\mathrm{Jup}}$ (Lovis et al. 2009). The exact fraction of stars with (hot) Neptune-sized planets remains in dispute, but transit data from the CoRoT and Kepler satellites will soon resolve this issue. Very little is known about the incidence of planets in the outer reaches of planetary systems because of small RV amplitudes, vanishing transit probabilities, and long orbital timescales. Imaging and microlensing (Gould & Loeb 1992; Bennett et al. 2007) provide probes of these systems with imaging offering the prospect of detailed follow-up observations. Previous imaging surveys on 8 m class telescopes provide

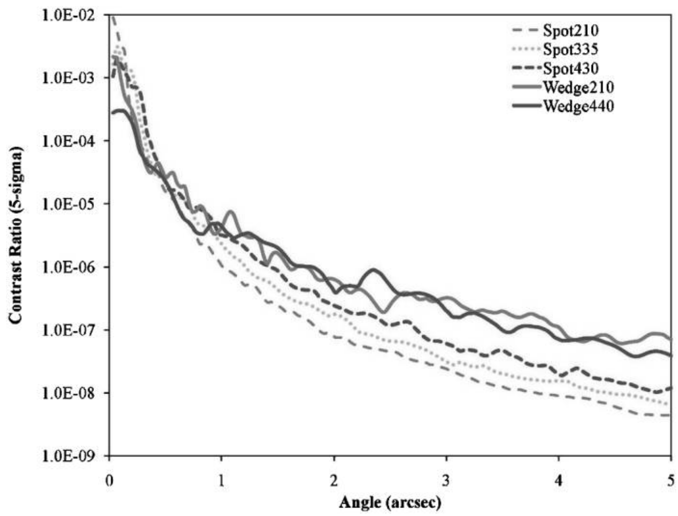

FIG. 6.—Contrast ratio (5σ) as a function of off-axis angle is shown for the various NIRCam coronagraph masks assuming subtraction of two rolls ($+5°$ and $-5°$) for speckle suppression. A position offset error of 10 mas and a wavefront error of 10 nm between rolls has been assumed. The two wedges are shown as *solid lines* and the three spots as *dash-dotted, dashed, and dotted lines* respectively are F430, F335, and F210. See the electronic edition of the *PASP* for a color version of this figure.

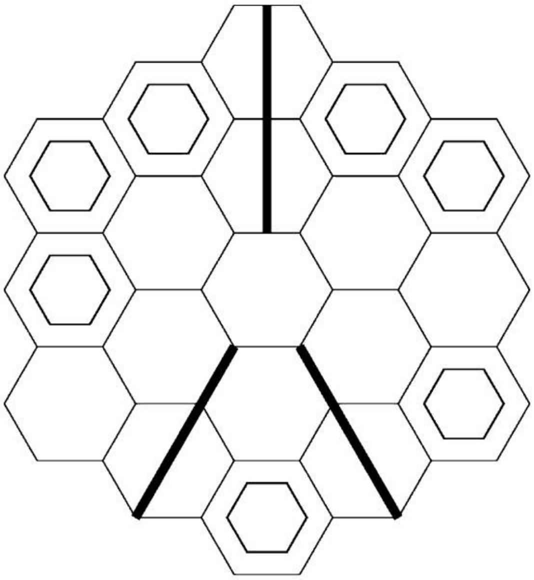

FIG. 7.—Layout of the subapertures, projected onto the *JWST* primary mirror for the nonredundant mask (NRM) interferometer (Sivaramakrishnan et al. 2009).

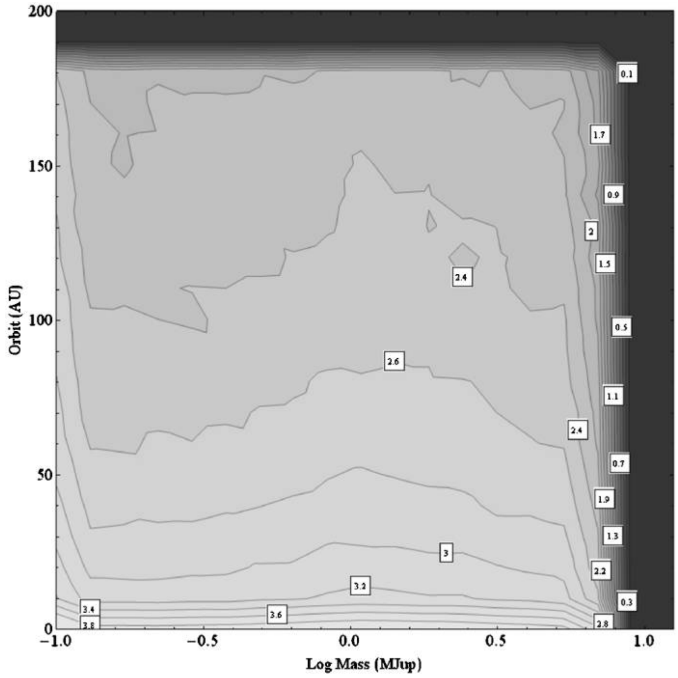

FIG. 8.—Distribution of planet masses and semimajor axes for a typical Monte Carlo run for the young stellar sample assuming $dN/da \propto a^{-1}$. As discussed in the text, the masses of planets orbiting M stars are capped at 2 $M_{\rm Jup}$ compared with 10 $M_{\rm Jup}$ and an enhanced population of ~2 $M_{\rm Jup}$ planets has been adopted for stars more massive than 1.5 $M_\odot$. The contours represent logarithmic intervals with arbitrary normalization. See the electronic edition of the *PASP* for a color version of this figure.

statistical constraints of $<25\%$ for the incidence of relatively massive planets ($>2\ M_{\rm Jup}$) on relatively large separations, 40–200 AU (Lafrenière et al. 2007; Biller et al. 2007).

For our simulation we have adopted a simplified model for the distribution of planets in the mass-SMA plane. We assume that every star has (only) one planet drawn from a distribution with an incidence $dN/dM \propto M^{-1}$ between 0.1 and 10 $M_{\rm Jup}$. The maximum mass for M stars is capped at 2 $M_{\rm Jup}$ to reflect the underabundance of massive planets for these stars (Johnson et al. 2007). Reflecting the growing evidence for an increased incidence of planets orbiting massive stars (Johnson 2008), we enhance the number of massive planets around stars with $M > 1.5\ M_\odot$ over the simple M^{-1} power law. For these stars we added a log-normal distribution of planets with a mean of 2 $M_{\rm Jup}$ and a factor of 2 dispersion in mass. The exact nature of this enhancement did not make a large difference in the simulation results. Based on the current census of exoplanets, we allowed $\eta = 20\%$ of the trials to place a planet between 0.1 and 5 AU. For the remaining $1 - \eta = 80\%$ of stars, we drew from a distribution in SMA (denoted by a) with $dN/da \propto a^{-1}$ between 5 and 200 AU which favors closer-in planets and thus represents a more difficult case for direct imaging. Figure 8 shows the distribution of planets in the mass-SMA plane and is similar to those adopted by Lafrenière et al (2007). We also investigated $dN/da \propto a^0$ to examine what range in orbital distributions might be detectable for comparison with alternative formation and/or migration mechanisms. Orbital eccentricities were drawn from a probability distribution function between $0 < e < 0.8$ derived from the observed distribution of eccentricities for 269 radial velocity planets with periods greater than 4 days (Cumming 2004; Schneider 2009 and references therein).

Our calculations require predictions of the brightness of planets at various wavelengths as functions of mass and age. One widely used group of models is the CONDO3/DUSTY models (Baraffe et al. 2003) which follow the evolution of a contracting planet. These models combine the evolution of effective temperature ($T_{\rm eff}$) and radius with a detailed atmospheric model to predict the appearance of planets across a wide range of wavelengths. Baraffe (2009, private communication) extended these models to include planets with masses as low as $0.1\ M_{\rm Jup}$ for this article. We used filter profiles for *JWST*/NIRCam and *JWST*/MIRI to produce magnitudes for planets in these passbands to augment what was already available for ground-based filters (Appendix A, Tables 10–19). As the color-magnitude diagrams indicate (Fig. 9), the predominant effect governing the appearance of a planet is its $T_{\rm eff}$ with considerable overlap in colors as objects of different mass pass through a particular temperature. The [4.4]–[11.4] color-magnitude diagram spreads out the effects between mass and age on $T_{\rm eff}$ and luminosity and may be useful in breaking these otherwise degenerate parameters.

There are, however, a number of caveats that should be considered when using these models. First, the physics underlying these models becomes unreliable at effective temperatures below 100 K. While this is not an issue for the *young* planets considered in § 6.1, the lack of good models for ~1 $M_{\rm Jup}$ planets

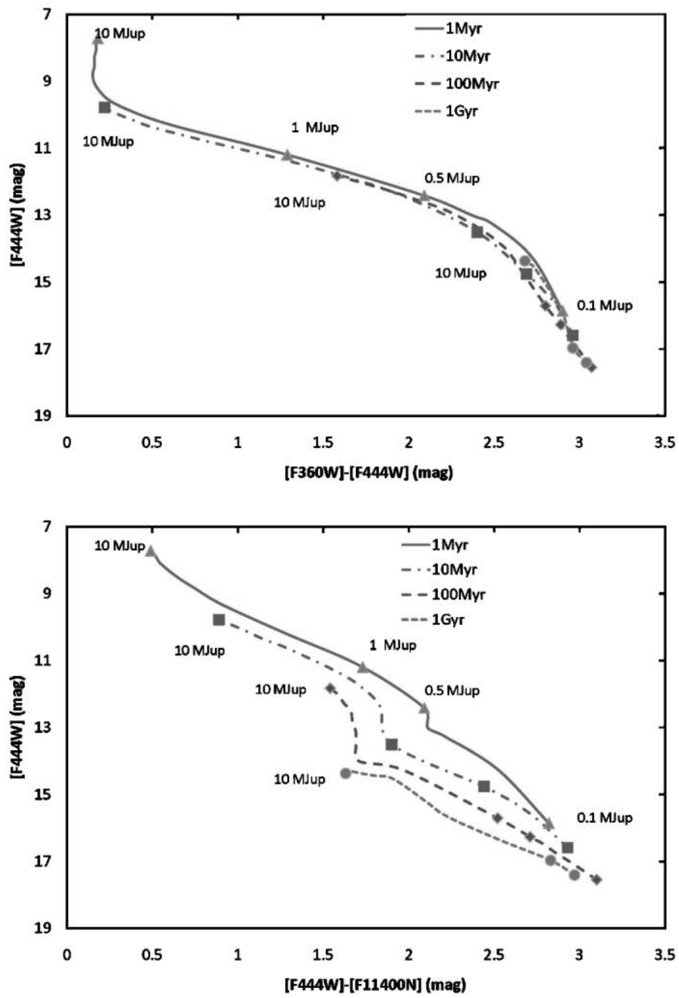

FIG. 9.—Color-magnitude diagrams for young planets using Baraffe (2003) models calculated for masses as low as $0.1\ M_{\rm Jup}$ with effective temperatures as low as 100 K. (*Top*) models in to near-IR bands observable with NIRCam or TFI/NRM; (*bottom*) models in bands observable with either NIRCam or TFI/NRM and MIRI. The combination of 5 and 11 μm colors appears to break the degeneracy between age and mass and may be valuable in assessing the evolutionary state of different planets. See the electronic edition of the *PASP* for a color version of this figure.

older than a few Gyr is a problem for the analysis of planets orbiting older M stars (§ 6.2). As will be discussed, the *JWST* instruments have the sensitivity needed to observe $1\ M_{\rm Jup}$ planets orbiting the nearest M stars at separations of a few AU. The lack of good models at the low temperatures of these objects makes these results qualitative.

Second, the Baraffe calculations are based on a so-called "hot-start" evolution which ignores the effects of core accretion. These effects have recently been identified as important for the earliest evolutionary phases of these planets (Marley et al. 2007). There can be significant differences between the luminosity and effective temperature between a planet forming through core accretion with an associated accretion shock versus simply following the gravitational contraction of a preexisting ball of gas of the same mass (the "hot-start" model). At very young ages, the core accretion systems can be 5–100 times fainter than simple hot-start model prediction. This effect is illustrated in Figure 10 for planets of 2 and $10\ M_{\rm Jup}$ in the 5 μm M band for the CONDO3 models used in this article (Baraffe et al. 2003) and for the core-accretion models (Fortney et al. 2008). The differences can be significant for young, massive planets: up to 3–5 magnitudes in M ([4.4 μm]) brightness at an age of 1 Myr for a $10\ M_{\rm Jup}$ planet. The differences are more modest, 1–2 magnitudes, for older, lower-mass planets, e.g., $1\text{–}2\ M_{\rm Jup}$ at ages of 10 Myr. We discuss a limited comparison between hot-start and core accretion models in § 6.1.1.

Irradiation by a central star can greatly modify a planet's appearance (Burrows et al. 2003; Baraffe et al. 2003), but is of limited importance for the systems considered here because of the large planet-star separations detectable with direct imaging. Furthermore, for young stars, the effect of irradiation at separations larger than a few AU is small in comparison to the planet's internal energy. In the case of NRM or FQPM imaging or observations with a 30–40 m telescope, the planets are close enough to their host stars (≲5 AU) that stellar irradiation can become modestly important. In this case we combined planet's intrinsic effective temperature, $T_{\rm Eff,int}$, with the additional energy from the star of luminosity L at a separation, a, assuming an albedo $= 0.1$ and complete redistribution of the absorbed radiation to arrive at a

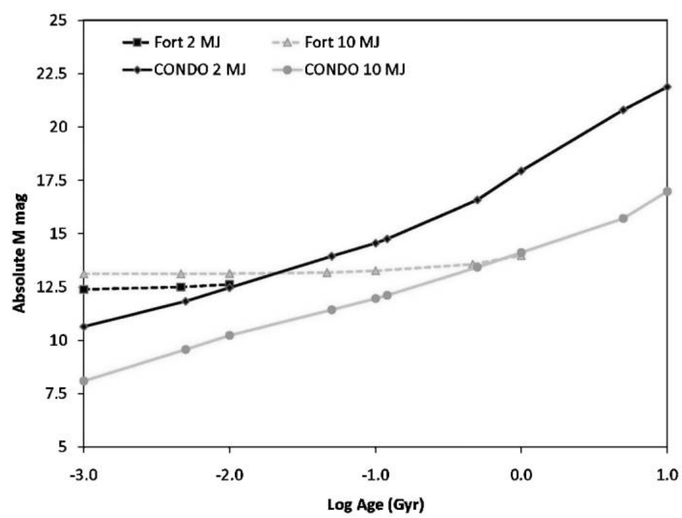

FIG. 10.—Comparison of two sets of evolutionary tracks for $1\ M_{\rm Jup}$ and $10\ M_{\rm Jup}$ planets. *Solid curves* represent the M [4.5 μm] brightness from the CONDO3 models (Baraffe et al. 2003) used in this article. *Dashed curves* represent the core-accretion models (Fortney et al. 2008), which are generally fainter at any given time. Thus a "core-accretion" planet of a certain brightness will be more massive by a factor of 2 or more than a planet following the "hot-start" contraction tracks. See the electronic edition of the *PASP* for a color version of this figure.

new, higher $T_{\rm Eff,new}$ for the planet. We then selected as our model for the planet's emission the model with the same mass but for a younger object having the newly calculated, elevated $T_{\rm Eff,new}$:

$$T_{\rm Eff,ext} = 270(1 - \text{albedo})^{0.25} L_{*,\odot}^{0.25} a_{\rm AU}^{-0.5}\ K, \quad (1)$$

$$T_{\rm Eff,new} = (T_{\rm Eff,int}^4 + T_{\rm Eff,ext}^4)^{0.25}. \quad (2)$$

5. THE MONTE CARLO SIMULATION

For a given instrument configuration (telescope, instrument, wavelength, contrast ratio as a function of off-axis angle) we selected a particular stellar sample: young stars (comprising the *SIM* YSO, FEPS, and A-star lists, § 2.1) or the nearby M stars (§ 2.2). We drew planets of random mass, semimajor axis and eccentricity according to the distributions described above. The planet's separation from its host star was weighted according to the time spent in the appropriate Keplerian orbit and randomized over all possible starting points and orientations. It should be noted that highly eccentric planets spend much of their time near apoastron and may thus peek outside the inner working angle of an instrument and be detectable for a fraction of their orbital period (Agol 2007; Brown 2009). For the large orbital separations of relevance here, the orbital periods are typically so long so that this effect is a static one over the duration of an individual survey, in contrast with the planets considered by Agol (2007) and Brown (2009), which investigate the changing effects of orbital motion on the changing visibility of habitable zone planets (~1–3 AU) orbiting stars within 10–15 pc.

Each star served as a seed for 1000 Monte Carlo runs. A planet was scored as a detection if it: (1) lay between the inner and outer working angles; (2) was above the 5σ sensitivity limit for an observation consisting of the difference between two 1 hr long integrations to account for a differential technique for speckle suppression, e.g., roll or PSF subtraction; and (3) was brighter than the 5σ floor set by the contrast ratio appro-

TABLE 5

YOUNG PLANET SIMULATIONS (ALL STARS)

(1) Inst.	(2) λ (μm)	(3) Num. Det	(4) Num (>25%)	(5) Avg. Score (%)	(6) Mass. ($M_{\rm Jup}$)	(7) Min ($M_{\rm Jup}$)	(8) SMA (AU)	(9) Min (AU)	(10) Age (Myr)	(11) RV[a] (%)	(12) Astr.[a] (%)
641 Young Stars, Orbit $\alpha = -1$											
NICI	1.65	349	0	7.0	5.9 ± 2.4	3.28	80 ± 31	30	15	0.03	0.68
P1640	1.65	428	12	10.0	5.7 ± 2.5	3.42	59 ± 28	16	26	0.21	2.31
GPI	1.65	535	57	12.9	5.0 ± 3.0	2.88	55 ± 26	13	31	0.39	3.09
TMT	1.65	602	334	28.4	4.1 ± 2.4	1.53	43 ± 12	3	44	2.86	12.32
NIRCAM Spot	3.56	632	58	11.8	2.6 ± 1.6	0.38	135 ± 22	65	53	0.00	0.26
MMT[c]	4.44	85	1	4.3	7.7 ± 2.6	6.25	80 ± 36	39	17	0.05	1.70
NIRCAM Spot	4.44	640	173	16.1	1.7 ± 0.9	0.18	130 ± 30	64	54	0.00	0.40
TFI/NRM	4.44	612	286	22.5	2.7 ± 2.1	0.67	22 ± 13	5	49	2.41	9.20
TFI/NRM NoCal[b]	4.44	419	15	10.1	5.0 ± 2.9	2.75	29 ± 13	8	17	0.55	3.36
MIRI	11.40	633	240	24.4	3.1 ± 1.9	0.57	93 ± 26	24	53	0.73	3.73
641 Young Stars, Orbit $\alpha = -1$, Randomized Ages											
P1640	1.65	412	15	11.0	5.5 ± 2.4	3.16	61 ± 27	16	25	0.20	2.40
NIRCAM	4.44	640	189	18.4	1.9 ± 1.0	0.18	121 ± 27	50	54	0.01	0.60
641 Young Stars, Orbit $\alpha = 0$											
NICI	1.65	388	27	10.7	5.2 ± 2.9	3.03	95 ± 32	32	14	0.01	0.20
P1640	1.65	421	45	12.0	5.6 ± 2.5	3.39	82 ± 35	20	25	0.08	0.76
GPI	1.65	504	101	14.1	5.4 ± 2.6	3.09	81 ± 35	17	35	0.15	1.04
TMT	1.65	600	306	27.0	4.1 ± 2.4	1.51	81 ± 24	3	43	1.88	5.22
MMT[c]	4.44	84	0	4.6	7.7 ± 2.4	6.16	105 ± 36	43	15	0.01	0.68
NIRCAM Spot	4.44	640	354	34.0	1.6 ± 0.8	0.14	140 ± 25	62	54	0.00	0.17
TFI/NRM	4.44	609	53	12.7	2.6 ± 2.0	0.70	31 ± 21	6	48	1.38	3.29
MIRI	11.40	637	465	37.0	2.7 ± 1.8	0.53	122 ± 18	27	53	0.41	1.28

NOTE.—Columns (1) and (2) identify the instrument; column (3) gives number of stars with at least one planet detection; column (4) gives number of stars with at least a >25% probability of detecting a planet; column (5) gives the average detectability averaged over all stars with at least one detection; columns (6) and (7) give average and minimum values of detected planet mass; columns (8) and (9) give average and minimum values of detected semimajor axes; column (10) gives average age of detected planets; columns (11) and (12) present detectability scores for imaged planets that were also detectable using either RV or *SIM* Lite astrometry.

[a] Percentage of sources detected via imaging also detectable with RV or astrometry.

[b] Without visibility calibration.

[c] Approximates the performance of a coronagraph on a telescope like the MMT as similar to that of NIRCam but with a magnitude floor of $M = 14$ mag.

priate to the apparent star-planet separation and stellar magnitude. Scores were kept for each star and for each mass-SMA bin. The simulations were run for different instrument configurations and for planet distributions with $dN/da \propto a^0$ and a^{-1} (Table 5 et seq.).

Detection of a companion to a bright star in a single sighting is not, of course, adequate to claim that a faint adjacent source is a planet. Verification of the planetary nature of the object requires observations at different epochs to detect common proper motion, orbital motion, or differential parallactic motion relative to nearby reference stars (Zimmerman 2010). This step will be a critical part of any realistic survey.

6. DISCUSSION

6.1. Results For Young Stars

Table 5 summarizes how the different instruments probe the planet mass-SMA parameter space with results given for two different assumptions about the distribution of planets, $dN/da \propto a^{-1}$ and a^0. In what follows we concentrate on the $\alpha = -1$ case. The effect of uncertain ages ($\times 2$ dispersion around the nominal age) was investigated for one ground-based and one space-based instrument, but did not make a significant difference to the outcome so long as the average value is preserved.

Table 5 presents Monte Carlo results averaged over the entire sample of 641 "young stars" as well as for the 25 stars achieving the highest detectability scores, i.e., the fraction of Monte Carlo draws resulting in a detected planet. Logarithmic averages of the mass and true SMA (not the apparent orbital separation) of the detected planets, as well as the average of the minimum detectable mass and SMA for each star, were calculated for each simulation. Average values of mass and semimajor axis for all detected planets are summarized by instrument in Figure 11 where the symbol size is proportional to the fractional detection rate and the "error bars" give the 1σ dispersion in mass and semimajor axis of the detected planets. Symbols are shown for the average over all stars in the young star sample and for the best 25 stars detected by each instrument.

Detailed information for each instrument and planet population is given in Tables 5 et seq. Columns (1)–(2) identify the sample and instrument; columns (3) and (4) give the number of stars with any detection of a planet and the number of stars with planets detected more than $>25\%$ of the time; column (5) gives the fraction of times a planet was detected, averaged over all stars having at least 1 detection; columns (6) and (7) give average and minimum values of detected planet mass; columns (8) and (9) give average and minimum values of detected planet semimajor axes; column (10) gives average age of detected planets; columns (11) and (12) present detectability scores for imaged planets that were also detectable using either RV or *SIM*-Lite astrometry (§ 6.2). The average values of mass and SMA include estimates of the dispersion in these quantities. Table 6 repeats this information but averages over only the ≤25 stars

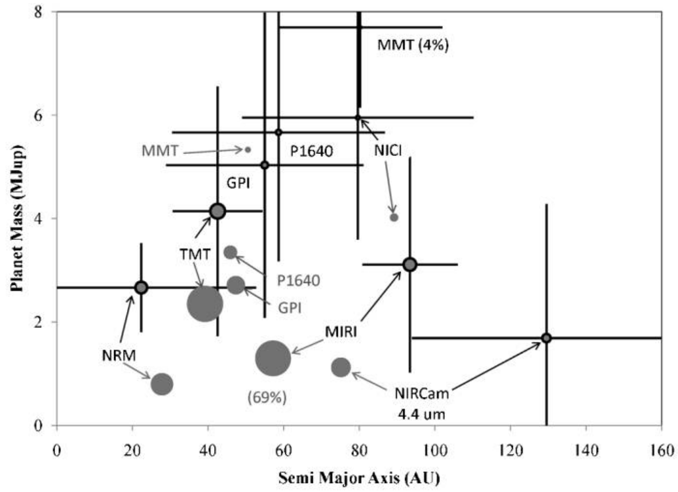

FIG. 11.—Average values of planet mass and semimajor axis for planets detected with each instrument as presented in Table 5. The size of the symbol is proportional the fraction of stars around which at least 1 planet was detected; the percentages corresponding to two representative symbol sizes are indicated. Vertical and horizontal bars denote the 1σ dispersion in these quantities. *Open circles* with error bars are for the samples averaged over all stars with detections with the error bars denoting the 1σ dispersion in the planetary properties. *Filled circles,* with the error bars omitted for clarity, denote the planet parameters averaged over the best 25 stars in each run. See the electronic edition of the *PASP* for a color version of this figure.

with the highest fraction of detections. Listings of the stars with the highest scores are presented in Appendix B (Tables 20–23) for reference. It should be noted that two recently imaged A stars with planets, Fomalhaut and HR 8799, both finished high in the rankings, e.g., with scores ~30% for NIRCam and ~5% for GPI, but were not among the top 25 targets in the simulations.

Figure 11 and Tables 5–6 suggest that ground-based coronagraphy with the next generation of instruments (P1640, GPI, SPHERE) should routinely detect planets larger than about 3–5 $M_{\rm Jup}$ within 20–50 AU with favorable cases yielding planets as small as 1 $M_{\rm Jup}$ or close as 15 AU. This information is shown graphically in Figure 12 et seq. for a number of instruments. In these and subsequent plots, the contours represent probability of detection of a planet in a specific mass-SMA bin, i.e., the number of planets detected in that bin divided by the total number of planets generated in that bin (Fig. 8). The initial discoveries of the planets orbiting HR 8799 and Fomalhaut (50–100 AU) are encouraging and suggest that with instrumental improvements, detections of planets much closer to the stars should become possible in this mass range. These results are consistent with predictions for GPI (Macintosh et al. 2006). M-band observations from the ground suffer from high thermal backgrounds, making such surveys somewhat unfavorable despite the brightness of young planets at this wavelength. In the longer term, interferometry with the Large Binocular Telescope Interferometer (LBTI) offers the prospect of

TABLE 6

YOUNG PLANET SIMULATIONS (BEST 25 STARS)

(1) Instr.	(2) λ (μm)	(3) Num. Det	(4) Num (>25%)	(5) Avg. Score (%)	(6) Mass ($M_{\rm Jup}$)	(7) Min ($M_{\rm Jup}$)	(8) SMA (AU)	(9) Min (AU)	(10) Age (Myr)	(11) RV (%)	(12) Astr. (%)
641 Young Stars, Orbit $\alpha = -1$											
NICI	1.65	349	0	15.9	4.0 ± 2.4	0.93	89 ± 31	24	2	0.00	0.17
P1640	1.65	428	12	26.1	3.3 ± 2.5	1.41	46 ± 28	9	8	0.22	10.18
GPI	1.65	535	57	35.4	2.7 ± 3.0	0.92	47 ± 26	8	5	0.45	12.51
TMT	1.65	602	334	69.7	2.4 ± 2.4	0.45	39 ± 12	1	13	2.10	35.62
NIRCAM Spot	3.56	632	58	36.5	1.4 ± 1.6	0.11	83 ± 22	15	39	0.03	3.28
MMT[3]	4.44	85	1	11.1	5.3 ± 2.6	3.20	51 ± 36	12	42	0.16	5.42
NIRCAM Spot	4.44	640	173	37.8	1.1 ± 0.9	0.10	75 ± 30	18	37	0.00	2.16
TFI/NRM	4.44	612	286	43.1	0.8 ± 2.1	0.12	28 ± 13	6	3	0.61	9.30
TFI/NRM NoCal[2]	4.44	419	15	25.9	2.4 ± 2.9	0.56	35 ± 13	7	2	0.17	4.08
MIRI	11.40	633	240	68.8	1.3 ± 1.9	0.10	57 ± 26	2	22	4.34	20.93
641 Young Stars, Orbit $\alpha = -1$, Randomized Ages											
P1640	1.65	412	15	29.8	3.0 ± 2.4	1.02	49 ± 27	9	10	0.29	9.49
NIRCAM	4.44	640	189	41.8	1.1 ± 1.0	0.10	71 ± 27	13	36	0.26	5.04
641 Young Stars, Orbit $\alpha = 0$											
NICI	1.65	388	27	29.0	3.4 ± 2.9	0.73	115 ± 32	25	1	0.00	0.00
P1640	1.65	421	45	32.8	3.3 ± 2.5	0.85	113 ± 35	22	2	0.00	0.13
GPI	1.65	504	101	40.7	2.7 ± 2.6	0.70	108 ± 35	17	2	0.00	0.29
TMT	1.65	600	306	63.8	2.3 ± 2.4	0.47	83 ± 24	2	9	0.46	13.63
MMT[3]	4.44	84	0	9.6	6.2 ± 2.4	3.86	88 ± 36	21	24	0.00	1.69
NIRCAM Spot	4.44	640	354	62.7	0.9 ± 0.8	0.10	119 ± 25	30	39	0.00	0.08
TFI/NRM	4.44	609	53	29.4	0.9 ± 2.0	0.15	55 ± 21	10	2	0.00	0.50
MIRI	11.40	637	465	79.8	1.1 ± 1.8	0.10	101 ± 18	2	25	3.11	7.54

NOTE.—Same as Table 5, but for an average over only those stars with the highest detection fraction (up to the 25 highest ranked targets).

examining nearby young stars with <50 mas resolution. Performance improvements possible with the LBTI will enhance the number of planets relative to the MMT values.

Given our assumptions about the planetary systems and the optimization of the survey, success rates for the next generation of ground-based surveys (GPI and P1640) could be as high as 25%–35% for an optimized H-band survey and 10% for an optimized M-band survey. Eventually, an advanced coronagraph on TMT (Fig. 13) could push this detection threshold up to ~70% at lower masses (~1–2 $M_{\rm Jup}$) and with minimum separations as small as a few AU for the most favorable stars.

JWST will detect lower mass planets that cannot be detected from the ground, with success rates of up to 40% for the best stars (Table 5). Operating at 3.6 or 4.4 μm (Fig. 14), NIRCam will have a broad plateau of $>30\%$ detection probability outside of 50 AU and $>50\%$ outside of 100 AU for masses down to $0.2\ M_{\rm Jup}$. Interior to 50 AU, the probability of detection drops rapidly except for the most massive planets. The NIRCam performance is similar at 3.6 μm and 4.4 μm, with the decrease in brightness of the planets offsetting the improved resolution at the shorter wavelength. The table confirms that the performance differences between NIRCam's Spot and Wedge-shaped masks are small, with a slight advantage for the Wedge to find closer-in planets. For the most favorable 25 stars, i.e., the closest and/or youngest, NIRCam can detect planets as small as $0.1\ M_{\rm Jup}$ or as close in as 15 AU. However, as a Lyot coronagraph operating on a telescope of modest size, NIRCam is not sensitive to the inner reaches of planetary systems.

The NRM imager (Fig. 15) operates with a small inner working angle and may find planets with an average orbital separation for the 25 best stars of 30 AU for masses as low as $0.8\ M_{\rm Jup}$. Planets as small as $0.1\ M_{\rm Jup}$ and orbital separations as small as 5–10 AU could be detected in the most favorable cases. This performance is limited to a small outer working angle and relies critically on achieving a stable visibility calibration. Without this calibration the predicted contrast ratio is $\sim 10\times$ worse and the TFI/NRM success ratio drops by a factor of $2 \sim 3$.

MIRI coronagraphy, as illustrated by the performance of the 11.4 μm FQPM (Fig. 16), will complement NIRCam and NRM imaging with its small inner working angle $(1\lambda/D)$ coupled with a large field of view (13″). For the 25 best stars, MIRI will have a 70% success rate in finding planets with average masses of 1–2 $M_{\rm Jup}$ at average separations of 60 AU; planets as small as $0.10\ M_{\rm Jup}$ and separations as small as <5 AU are possible.

It must be emphasized that these "success rates" depend on each telescope and instrument combination achieving its nominal performance (contrast ratio and sensitivity) and on the as-

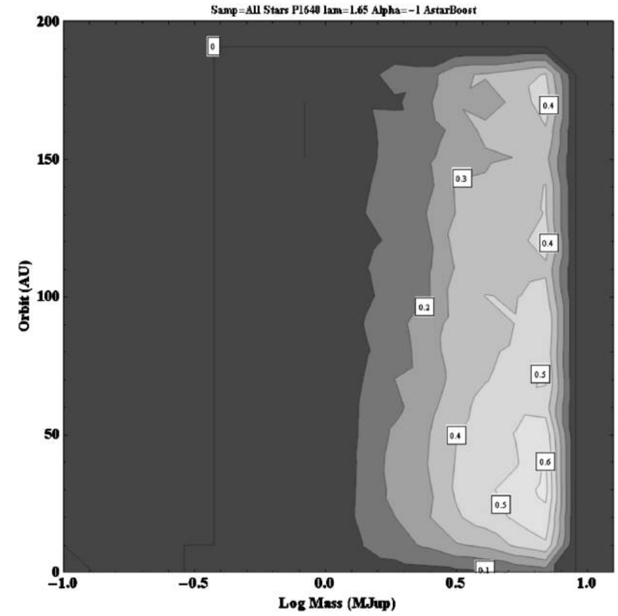

FIG. 12.—Fractional detectability of planets orbiting nearby young stars ($\alpha = -1$) for the P1640 coronagraph operating at 1.65 μm. The vertical axis represents orbital semimajor axis (AU) and the horizontal axis Log(planet mass) (in $M_{\rm Jup}$). A comparable instrument operating on an 8 m telescope (GPI/SPHERE) would find planets at $5/8\times$ smaller separations. The contours (displayed in white boxes) represent the probability of detection of a planet, averaged over all stars, in a specific Mass-SMA bin, i.e., the number of planets detected in that bin divided by the number of planets generated in the simulation. See the electronic edition of the *PASP* for a color version of this figure.

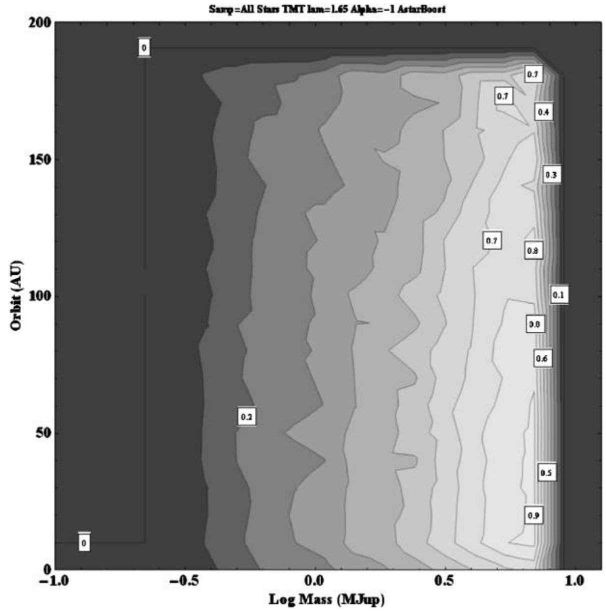

FIG. 13.—Fractional detectability of planets orbiting nearby young stars for a coronagraph operating at 1.65 μm on a 30 m telescope (TMT). The vertical axis represents orbital semimajor axis (AU) and the horizontal axis Log(planet mass) (in $M_{\rm Jup}$). The contours represent the probability of detection of a planet, averaged over all stars, in a specific Mass-SMA bin, i.e., the number of planets detected in that bin divided by the number of planets generated in the simulation. See the electronic edition of the *PASP* for a color version of this figure.

sumptions implicit in the population of planets, e.g., at least 1 planet per system with a particular distribution of masses and orbits. Until each instrument is brought into operation, these results must be considered highly preliminary. This is particularly the case for the innovative modes on *JWST*, e.g., TFI/NRM and MIRI FQPM, where large extrapolations in performance are being made compared with the current state of the art.

These results, summarized by stellar host properties (Figs. 17 and 18) reveal interesting differences between the instruments. The top portion of Figure 17 compares the performance of NIRCam and TFI/NRM at 4.4 μm. The NIRCam coronagraph does the best job on the closest stars whose more mature planets require the highest contrast ratio. Some of the best targets for TFI/NRM are relatively distant young stars where NRM's high angular resolution brings luminous 10 Myr old planets into view that are hidden from other instruments. The bottom panel of this figure adds MIRI into the comparison which largely displaces TFI/NRM by doing a good job of finding the youngest planets at all stellar distances. Figure 17 shows only the highest-scoring instrument for each star. In fact, there is good overlap in instrument scores in most cases, suggesting that it will be possible to characterize these planets at many wavelengths leading, possibly, to determinations of $T_{\rm eff}$ and radius (Fig. 9).

The distributions of spectral types with high detection fractions are shown for representative ground-based (P1640 at

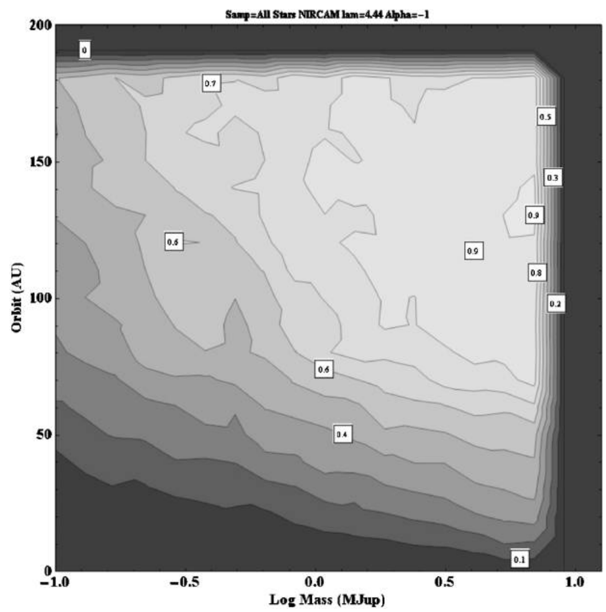

FIG. 14.—Fractional detectability of planets orbiting nearby young stars ($\alpha = -1$) for the NIRCam coronagraph at 4.4 μm. The vertical axis represents orbital semimajor axis (AU) and the horizontal axis Log(planet mass) (in $M_{\rm Jup}$). The contours represent the probability of detection of a planet, averaged over all stars, in a specific Mass-SMA bin, i.e., the number of planets detected in that bin divided by the number of planets generated in the simulation. See the electronic edition of the *PASP* for a color version of this figure.

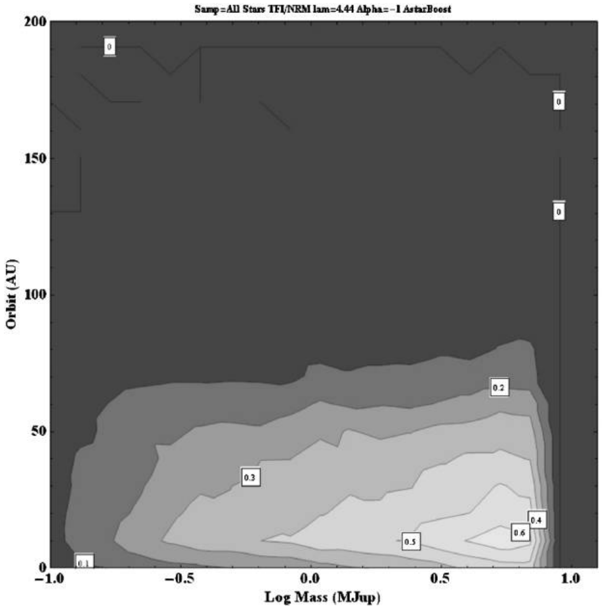

FIG. 15.—Fractional detectability of planets orbiting nearby young stars ($\alpha = -1$) for the TFI/NRM imager at 4.4 μm. The vertical axis represents orbital semimajor axis (AU) and the horizontal axis Log(planet mass) in (M_{Jup}). The contours represent the probability of detection of a planet, averaged over all stars, in a specific Mass-SMA bin, i.e., the number of planets detected in that bin divided by the number of planets generated in the simulation. The restriction to small separations is due to the restricted field of view of the NRM imager. See the electronic edition of the *PASP* for a color version of this figure.

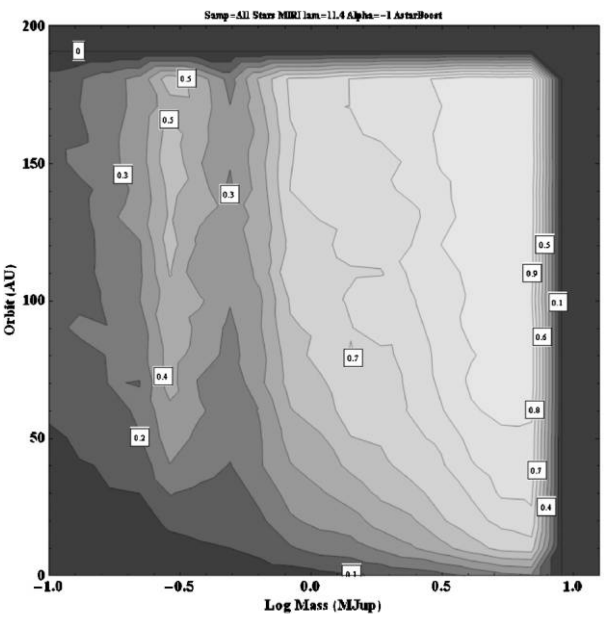

FIG. 16.—Fractional detectability of planets orbiting nearby young stars ($\alpha = -1$) for the MIRI/FQPM interferometer at 11.4 μm. The vertical axis represents orbital semimajor axis (AU) and the horizontal axis Log(planet mass) in (M_{Jup}). The contours represent the probability of detection of a planet, averaged over all stars, in a specific Mass-SMA bin, i.e., the number of planets detected in that bin divided by the number of planets generated in the simulation. See the electronic edition of the *PASP* for a color version of this figure.

1.65 μm) and space-based instruments (NIRCam at 4.4 μm). The spectral types of the entire young star sample are shown in the wide bins. The top ranked 100 stars in the Monte Carlo simulations are shown in the narrow bins for NIRCam with a fractional detectability score of $>29\%$ and for P1640, with a score of $>16\%$). Highly-ranked NIRCam targets span the full range of input spectral types with an average age of 10^8 yr, whereas young ($10^{6.8}$ yr) K and M stars at the low-mass end and high-mass A stars dominate the P1640 rankings.

The top panel of Figure 19 compares the planetary detections for the three *JWST* instruments and shows that NIRCam does best for planets more distant than 40 AU with average masses as low as $<1\ M_{\rm Jup}$. MIRI operates over a comparable range of orbital distances and mass limit. TFI/NRM operates uniquely in

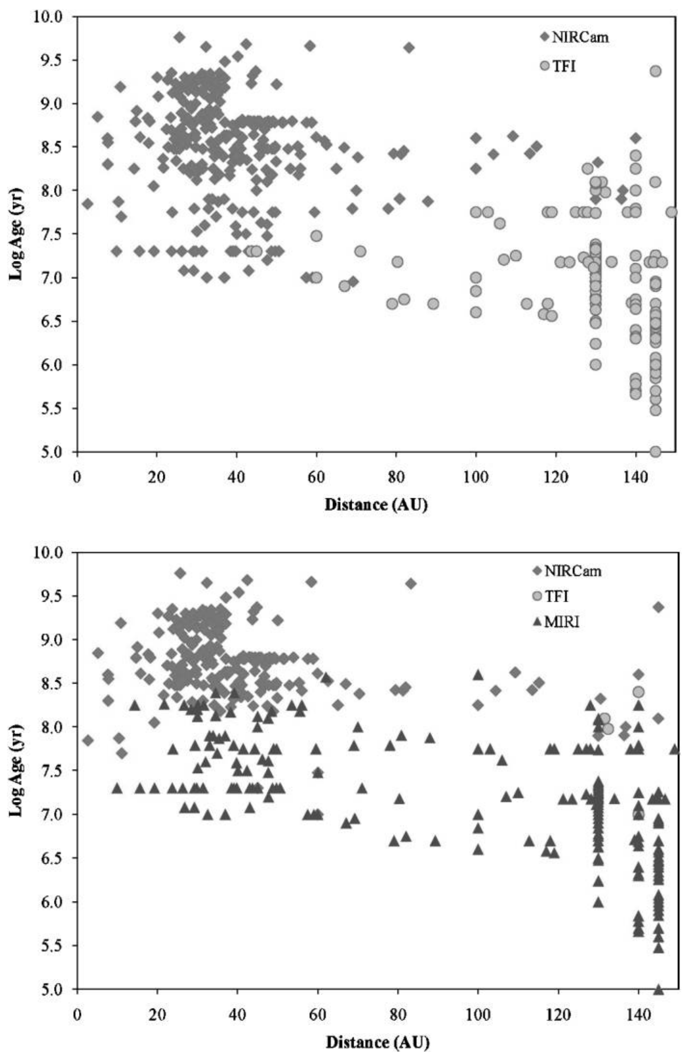

FIG. 17.—(*Top*) The instrument achieving the highest detectability score for the young stars sample ($\alpha = -1$) is shown on a star-by-star basis in the distance-age plane for *JWST*'s NIRCam and TFI/NRM at 4.4 μm. (*Bottom*) Comparable plot but for with the addition of MIRI at 11.4 μm. See the electronic edition of the *PASP* for a color version of this figure.

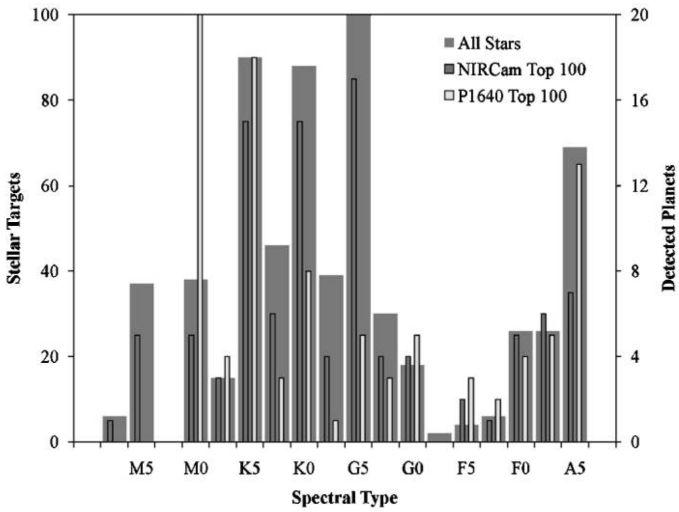

FIG. 18.—*Left hand scale,* histogram bins denote the distribution of spectral types for the 641 stars in the young star sample. *Right hand scale,* bins give the distribution of the top 100 ranked stars detected by NIRCam and P1640, respectively, for the $\alpha = -1$ planet distribution. See the electronic edition of the *PASP* for a color version of this figure.

the 10–20 AU range for the closest stars and overlaps with MIRI in the 40–50 AU range for younger, more distant stars. The two vertical bands of NRM detections highlight the two subsamples of young stars, i.e., 25–50 pc and 100–140 pc. The bottom panel compares present and future capabilities from the ground (P1640/GPI/SPHERE vs. TMT). While P1640/GPI will find planets >3–5 $M_{\rm Jup}$ and SMA >25–50 AU, an eventual TMT coronagraph will be able to probe to within 20 AU for considerably lower masses. *JWST*'s TFI/NRM and MIRI/FQPM perform well compared with TMT because they operate at 0.5–$1.0\lambda/D$, in comparison with 2.5–$4\lambda/D$ for a classical coronagraph. The change in inner working angle cancels much of the advantage of shorter wavelength and larger telescope diameter. The increased brightness of planets at 4 μm compared to 1.65 μm also contributes to *JWST*'s performance despite its smaller size.

The high success fractions for the *JWST* instruments suggests that at the completion of modest sized surveys, $25 \sim 50$ stars, it should be possible to test some of the assumptions made in this simulation: overall fraction of young stars with planets exterior to 5 AU, "hot-start" vs. "core accretion" evolutionary tracks, and orbital distribution with particular emphasis on the existence of planets on distant orbits. For example, the data obtained with *JWST* should suffice to distinguish between $dN/da \propto a^0$ and a^{-1} with a significant difference in the predicted average SMA between the two cases (Table 6). Figure 20 shows the cumulative yield of planets from different instruments in surveys of the most highly ranked stars. A survey of 50 stars with P1640, *JWST*/NIRCam, TFI/NRM, MIRI, and TMT would yield 12, 18, 21, 31, and 31 planets, respectively, for $\alpha = -1$ model and the assumption that there is one planet per star. In the case of *JWST*/NIRCam, the difference in the average value of the semimajor axis between the $\alpha = -1$ and 0 cases is highly significant, 81 ± 3 AU versus 120 ± 1 AU. For *JWST* and TMT, this result would remain significant, with only half the stars having planets instead of the assumed 100%. While this is not a definitive examination of parameter extraction from the simulations, this result suggests that surveys that can be accomplished in reasonable amounts of telescope time will address some of the key questions about the populations of planets in the outer reaches of these planetary systems.

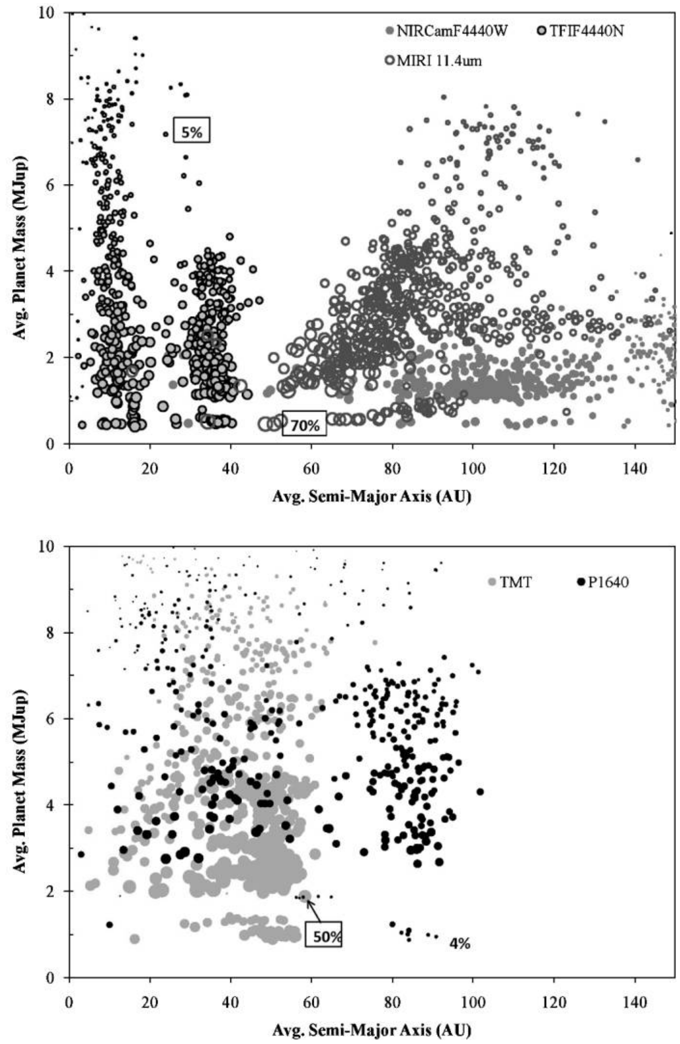

FIG. 19.—(*Top*) Average mass and semimajor axis (SMA) detected for each star in the young star sample ($\alpha = -1$) is shown with the size of the point proportional the fractional detectability of planets around that star (the percentages in boxes denote the achieved success rate corresponding to the adjacent symbol size). Results for three *JWST* instruments are shown: NIRCam and TFI/NRM at 4.4 μm, MIRI at 11.4 μm. (*Bottom*) Comparable plot for P1640 and TMT at 1.65 μm. For GPI and SPHERE on 8 m telescopes, the black dots would shift inward by roughly a factor of $5/8$ in orbital radius. The detections below $\sim$1 $M_{\rm Jup}$ correspond to planets orbiting young M stars for which the contrast ratio is particularly favorable. See the electronic edition of the *PASP* for a color version of this figure.

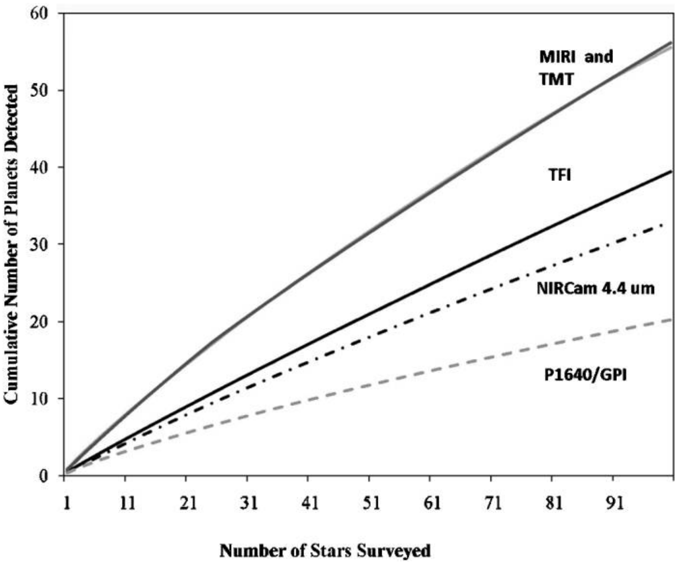

FIG. 20.—Cumulative number of planets detected as a function of the number of stars surveyed for the $\alpha = -1$ young star sample for different instruments. The stars are rank ordered according to the score in the Monte Carlo simulation (Appendix B). See the electronic edition of the *PASP* for a color version of this figure.

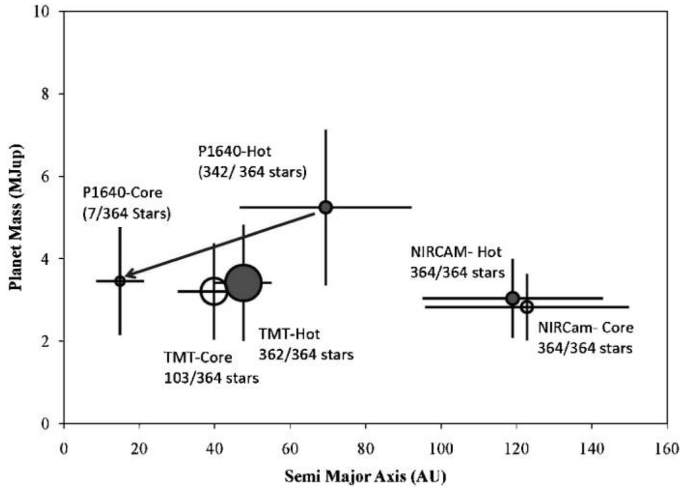

FIG. 21.—Average values of planet mass and semimajor axis for planets detected with P1640, TMT and NIRcam (Table 7) for the "hot-start" (Baraffe et al. 2003) and "core accretion" (Fortney et al. 2008; Marley et al. 2007) evolutionary scenarios. Stellar ages are less than 100 Myr and planet masses restricted to 1–10 $M_{\rm Jup}$. The most dramatic change comes for P1640 class instruments for which detectability drops to very small numbers. TMT and NIRCam have sensitivity to detect planets in this age-mass range with some independence of the evolutionary model; lower mass planets would start to become hard to detect however. The size of the symbol is proportional the fraction of stars around which at least 1 planet was detected. The vertical and horizontal bars denote the 1σ dispersion in these quantities. See the electronic edition of the *PASP* for a color version of this figure.

The addition of spectroscopic follow-up observations will provide insights into the physical properties of individual objects, while the addition of dynamical measurements will make these tests of theory much more stringent (§ 6.3).

6.1.1. "Core-Accretion" versus "Hot-Start" Models

An important consideration for young planets is that the assumed "hot-start" evolutionary models (Baraffe et al. 2003) may not be correct. As mentioned in § 4, planets formed by "core accretion" may be considerably fainter (Marley et al. 2007; Fortney et al. 2008) than the "hot-start" models used here. We investigated these differences for planets between 1–10 $M_{\rm Jup}$ and ages from 1–100 Myr (Table 2 in Fortney et al. 2008) for which comparable magnitudes are available for both sets of evolutionary tracks. We calculated Monte Carlo simulations for three cases (Table 7, Fig. 21): two ground-based systems, P1640 and TMT at 1.65 μm, and *JWST*/NIRCAM at 4.4 μm. The drop-off in the number of stars with planets is most marked with P1640 at 1.65 μm. The lower temperature at each age-mass point in the Fortney models affects the planet magnitudes dramatically, lowering the number of stars with at least one planet detection from 324 to 7 out of a total sample of 364 stars. For the more sensitive TMT observations, the drop-off is not so severe, from 362 to 103 stars with planets. NIRCAM at 4.4 μm is not affected by the change in planet brightness for two reasons. First, as mentioned, the differences are muted at longer wavelengths. Second, NIRCam's sensitivity is such that it can detect planets at 1 $M_{\rm Jup}$ for either evolutionary model. NIRCam would lose the ability to detect core-accretion planets of still lower mass or orbiting older stars, but the lack of Fortney models for these cases prevents us from discussing this quantitatively.

Another effect may mitigate the "hot start" versus "core accretion" problem. Planets located beyond 10 AU (the majority of those detectable via direct imaging) may not form via core accretion, but rather (at least in part) by gravitational fragmentation in the disk (Boss 2000). These planets may in fact be well represented by the "hot-start" models. Slight evidence for this hypothesis comes from fact that Fomalhaut b cannot have a mass much greater than 3 $M_{\rm Jup}$ lest it perturb the Fomalhaut ring (Kalas et al. 2008; Chiang et al. 2009). A core-accretion planet would have to be considerably more massive than this to have the observed brightness at the assumed age of Fomalhaut. The "hot-start" model may not prove to be a bad representation for the planets on the distant orbits that direct imaging will detect.

6.2. Results For Nearby M Stars

Our Monte Carlo simulations (Table 8) suggest that *JWST* (and to a lesser extent TMT) will be sensitive to self-luminous planets orbiting the nearest M stars at orbital distances beyond 10–20 AU. These results are unfortunately tentative due to the

TABLE 7

YOUNG PLANET SIMULATIONS: HOT-START VERSUS CORE-ACCRETION MODELS

(1) Instr.	(2) λ (μm)	(3) Num. Det	(4) Num (>25%)	(5) Avg. Score (%)	(6) Mass (M_{Jup})	(7) Min (M_{Jup})	(8) SMA (AU)	(9) Min (AU)	(10) Age (Myr)
P1640-Hot Start	1.65	324	152	40.9	3.7 ± 1.9	1.51	42 ± 23	7	9
P1640-Core Accretion	1.65	7	2	16.9	3.5 ± 1.3	2.18	15 ± 6	4	33
TMT-Hot Start	1.65	362	353	93.0	2.5 ± 1.4	1.00	44 ± 7	1	15
TMT-Core Accretion	1.65	103	87	76.0	3.4 ± 1.2	1.33	36 ± 10	1	17
NIRCAM-Hot Start	4.44	364	110	47.9	2.6 ± 1.0	1.01	69 ± 24	14	24
NIRCAM-Core Accretion	4.44	364	111	48.4	2.7 ± 0.8	1.01	70 ± 27	13	30

NOTE.—Columns are the same as in Table 5 but for systems with ages less than <100 Myr and planets with masses between 1–10 M_{Jup}.

inadequacy of the coldest, lowest mass models with effective temperatures below 100 K. Although we bounded the upper end of the mass range for M star planets at 2 M_{Jup} due to the apparent dearth of high-mass planets around low-mass stars, high-mass planets (5–10 M_{Jup}) would be easy to detect.

NIRCam is sensitive to planets orbiting nearby M stars having masses as low as 0.5 M_{Jup} and located at an average separation of $30 \sim 40$ AU (Fig. 22 and Tables 8–9), with considerably closer and smaller-mass planets being detectable for the most favorable stars (≲0.5 M_{Jup} and ~4 AU). TFI/NRM should be able to detect planets of comparable mass, but on orbits as proximate as 1–5 AU for younger, more distant M stars with X-ray derived ages $<10^8$ yr. MIRI/FQPM should detect planets as small as 0.5 M_{Jup} and ~40 AU with detections of higher mass objects possible at distances as close in as 3–5 AU (Fig. 23). With such small orbits, these planets might also be detectable with RV or astrometric measurements. A 0.5 M_{Jup} planet in a 5 AU orbit (22 yr period) around a 0.25 $M_\odot$ star at a distance of 10 pc would have radial velocity and astrometric amplitudes of 13 m s^{-1} and 100 μas, respectively. The combined imaging and dynamical observations would anchor planetary evolutionary models for ages of ~1 Gyr or more (§ 6.3).

From the ground at 1.65 μm, the sensitivity of the current (NICI) or even next generation of ground-based coronagraphs

TABLE 8

M STAR SIMULATIONS (ALL STARS)

(1) Instr.	(2) λ (μm)	(3) Num. Det	(4) Num (>25%)	(5) Avg. Score (%)	(6) Mass (M_{Jup})	(7) Min (M_{Jup})	(8) Min (AU)	(9) Min (AU)	(10) Age (Myr)	(11) RV[a] (%)	(12) Astr[a] (%)
196 M Stars, Orbit $\alpha = -1$											
NICI	1.65	7	0	3.8	1.6 ± 0.4	1.22	15 ± 7	11	20	0.09	2.57
P1640	1.65	15	1	6.8	1.6 ± 0.4	1.21	9 ± 3	3	38	1.27	5.49
GPI	1.65	17	1	9.7	1.4 ± 0.5	0.96	11 ± 4	2	43	2.00	7.48
MMT[b]	4.44	11	1	9.2	1.5 ± 0.3	1.17	21 ± 9	4	65	0.67	4.49
TMT	1.65	29	10	16.6	0.8 ± 0.7	0.50	10 ± 7	1	160	4.02	11.17
NIRCAM Spot	4.44	196	196	37.3	0.5 ± 0.1	0.10	34 ± 12	8	2,044	0.92	10.82
TFI/NRM	4.44	196	12	14.7	0.6 ± 0.2	0.14	4 ± 1	1	2,044	11.66	14.64
MIRI	11.40	196	67	25.6	0.8 ± 0.2	0.32	48 ± 18	4	2,044	2.91	10.15
196 M Stars, Orbit $\alpha = 0$											
NICI	1.65	4	0	2.1	1.4 ± 0.3	0.93	19 ± 9	7	13	0.10	1.50
P1640	1.65	12	0	4.2	1.5 ± 0.4	1.10	10 ± 6	2	33	1.68	3.50
GPI	1.65	17	0	4.7	1.4 ± 0.5	0.97	8 ± 5	2	43	2.21	3.85
TMT	1.65	29	1	9.4	1.0 ± 0.6	0.60	12 ± 10	0	162	3.85	5.96
MMT[b]	4.44	11	0	4.6	1.5 ± 0.3	1.18	30 ± 16	6	65	0.65	1.45
NIRCAM Spot	4.44	196	97	24.0	0.5 ± 0.1	0.10	46 ± 16	9	2,044	0.56	3.10
TFI/NRM	4.44	196	0	11.5	0.6 ± 0.2	0.13	3 ± 1	1	2,044	10.41	11.45
MIRI	11.40	196	39	22.1	0.8 ± 0.2	0.31	74 ± 25	6	2,044	2.50	4.69

NOTE.—Columns (1) and (2) identifies the instrument; column (3) gives number of stars with at least one planet detection; column (4) gives number of stars with at least a >25% probability of detecting a planet; column (5) gives the average detectability averaged over all stars with at least one detection; columns (6) and (7) give average and minimum values of detected planet mass; columns (8) and (9) give average and minimum values of detected semimajor axes; column (10) gives average age of detected planets; columns (11) and (12) present detectability scores for imaged planets that were also detectable using either RV or *SIM* Lite astrometry.

[a] Percentage of sources detected via imaging also detectable with RV or astrometry.

[b] Approximates the performance of a coronagraph on a telescope like the MMT as similar to that of NIRCam but with a magnitude floor of $M = 14$ mag.

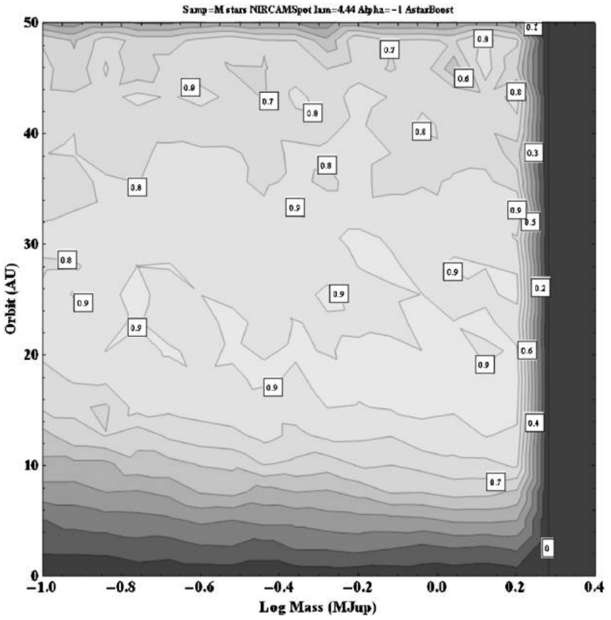

FIG. 22.—Ability for NIRCam to detect planets orbiting nearby M stars at 4.4 μm. The vertical axis represents orbital semimajor axis (AU) and the horizontal axis Log(planet mass) in ($M_{\rm Jup}$). The contours represent the probability of detection of a planet, averaged over all stars, in a specific Mass-SMA bin, i.e., the number of planets detected in that bin divided by the number of planets generated in the simulation. NIRCam can detect planets uniformly across the mass range 0.1–2 $M_{\rm Jup}$ assumed in the simulation but their detectability drops off at distances beyond 50 AU which falls outside the 10″ field of view for stars beyond 5–10 pc. See the electronic edition of the *PASP* for a color version of this figure.

(P1640, GPI, SPHERE) is probably inadequate to find mature planets around nearby M stars. The average score for these observing systems ranges from 3%–10% for the few of the youngest M stars with any detections at all. The greater collecting area and angular resolution of the TMT improves the prospects for success (up 20% in the most favorable cases), but the intrinsic faintness of older planets at short wavelengths will be difficult to overcome.

As indicated in the tables, we investigated both $\alpha = -1$ and $\alpha = 0$ power-law distributions of orbits. In contrast with the case of young stars, there is relatively little effect of the changing orbital separation, suggesting that angular resolution is not the dominant factor preventing detection of these planets, but rather that sensitivity is the bigger problem. In fact, the broader distribution ($\alpha = 0$) led to a modest *decrease* in the number of planets detected for the simple reason of running out of field of view in the instruments considered in the simulations; e.g., a 10″ field at 10 pc corresponds to 100 AU, which is only half of the 200 AU outer limit considered herein.

Finally, we note that the nearest M stars offer an alternative prospect for imaging planets, i.e., detection using *reflected* starlight. Depending on the ultimate performance of the *JWST* telescope at short wavelengths ($\lesssim 2$ μm), the NIRCam coronagraph might be able to find such planets around the few M stars within 5 pc, e.g., GJ 411 (Lalande 21185) at 2.5 pc where *JWST*/NIRCam's inner working angle of 0.28″ at 2.1 μm corresponds to 0.7 AU (Table 3). The brightness of a Jupiter at separation a in reflected light corresponds to a contrast ratio of $10^{-7} \sim 10^{-8} a_{\rm AU}^{-2}$ (depending on albedo and phase function) which will be

TABLE 9

M STAR SIMULATIONS (BEST 25 STARS)

Instr. (1)	λ (μm) (2)	Num Det (3)	Num (>25%) (4)	Avg. Score (%) (5)	Mass ($M_{\rm Jup}$) (6)	Min ($M_{\rm Jup}$) (7)	SMA (AU) (8)	Min (AU) (9)	Age (Myr) (10)	RV (%) (11)	Astr. (%) (12)
196 M Stars, Orbit $\alpha = -1$											
NICI	1.65	7	0	3.8	1.6 ± 0.4	1.22	15 ± 7	11	20	0.09	2.57
P1640	1.65	15	1	6.8	1.6 ± 0.4	1.21	9 ± 3	3	38	1.27	5.49
GPI	1.65	17	1	9.7	1.4 ± 0.5	0.96	11 ± 4	2	43	2.00	7.48
MMT	4.44	11	1	9.2	1.5 ± 0.3	1.17	21 ± 9	4	65	0.67	4.49
TMT	1.65	29	10	19.2	1.0 ± 0.7	0.59	12 ± 7	1	106	4.63	12.92
NIRCAMSpot	4.44	196	196	43.3	0.5 ± 0.1	0.10	29 ± 12	6	478	1.00	14.24
TFI/NRM	4.44	196	12	24.7	0.5 ± 0.2	0.11	5 ± 1	1	923	15.58	24.37
MIRI	11.40	196	67	79.0	0.5 ± 0.2	0.11	35 ± 18	1	93	9.02	32.97
196 M Stars, Orbit $\alpha = 0$											
NICI	1.65	4	0	2.1	1.4 ± 0.3	0.93	19 ± 9	7	13	0.10	1.50
P1640	1.65	12	0	4.2	1.5 ± 0.4	1.10	10 ± 6	2	33	1.68	3.50
GPI	1.65	17	0	4.7	1.4 ± 0.5	0.97	8 ± 5	2	43	2.21	3.85
TMT	1.65	29	1	10.8	1.1 ± 0.6	0.58	14 ± 10	1	114	4.43	6.88
MMT	4.44	11	0	4.6	1.5 ± 0.3	1.18	30 ± 16	6	65	0.65	1.45
NIRCAMSpot	4.44	196	97	34.0	0.5 ± 0.1	0.10	63 ± 16	13	2,630	0.00	0.91
TFI/NRM	4.44	196	0	18.0	0.4 ± 0.2	0.10	3 ± 1	1	500	14.16	17.93
MIRI	11.40	196	39	67.7	0.5 ± 0.2	0.12	65 ± 25	1	78	9.04	17.42

NOTE.—Same as Table 5, but for an average over only those stars with the highest detection fraction (up to the 25 highest ranked targets).

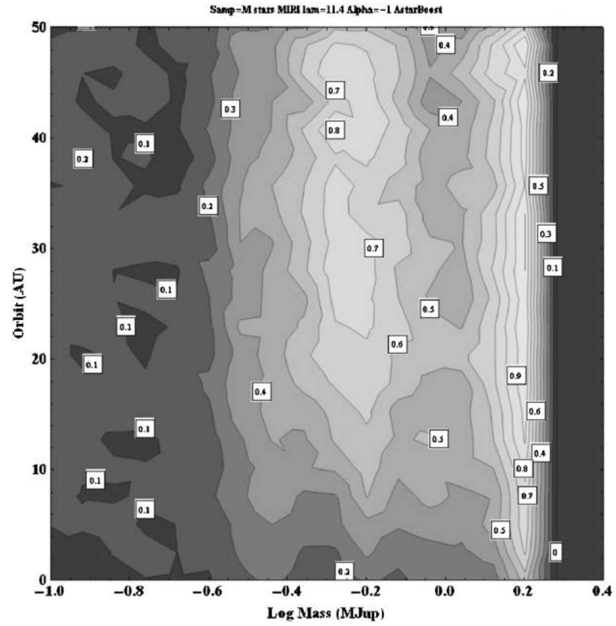

FIG. 23.—Ability for MIRI to detect planets orbiting nearby M stars at 11.4 μm. The vertical axis represents orbital semimajor axis (AU) and the horizontal axis Log(planet mass) in ($M_{\rm Jup}$). The contours represent the probability of detection of a planet, averaged over all stars, in a specific Mass-SMA bin, i.e., the number of planets detected in that bin divided by the number of planets generated in the simulation. The vertical locus at of contours represent M stars younger than 100 Myr for which <1 $M_{\rm Jup}$ planets can be detected while the second locus ($\log(M) \sim +0.2$) represents older stars for which only more massive planets can be detected. The detectability of planets drops off at distances beyond 50 AU due to the 13″ field of view for stars beyond 5–10 pc. See the electronic edition of the *PASP* for a color version of this figure.

difficult to achieve at 1″ (Fig. 6). More probably, it will take an extremely capable AO coronagraph; e.g., a 10^{-8} system on a 30 m telescope on the ground or a TPF-C telescope in space will be able to push into the domain of reflected light systems. A discussion of these prospects is beyond the scope of this article. The reader is referred to Agol (2007) or Brown (2009) for a detailed examination of detection of planets via reflected light.

6.3. Obtaining Masses via Dynamical Measurements

A dynamical technique is needed to determine the masses of planets detected via imaging. Estimates based on interactions with dust disks provide an indication of planet mass, e.g. Fomalhaut (Chiang et al. 2009), but radial velocity or astrometry can provide more definitive information, particularly if a near-complete orbit can be monitored. But both techniques are challenging and no young planets on even the closest <0.1 AU orbits, i.e., "hot Jupiters," have yet been found definitively via RV. Setiawan et al. (2008) have claimed an RV detection of a planet orbiting TW Hya, but this claim has been called into question as being due to large-scale photospheric variations (Huélamo et al. 2008). The result remains controversial. Similarly, Prato et al. (2008) identified potential "hot Jupiters" orbiting DN Tau and V836 Tau based on visible spectroscopy, but used follow-up IR spectroscopy to demonstrate that the variations were due to photospheric variability, not planets. Astrometry can find young gas giant planets; e.g., a Saturn-mass planet in a 5 AU orbit at 140 pc would have an astrometric amplitude of 12 μas and would be readily detectable with *SIM* Lite (Beichman 2001; Tanner et al. 2007; Unwin et al. 2008) and larger planets orbiting more nearby stars would be detectable with GAIA (Sozzetti et al. 2008) or ground-based interferometry at the 100 μas level (Van Belle et al. 2008; Pott et al. 2008).

We investigated the prospects for indirect detection by positing *single measurement* capabilities of 1 $\mathrm{m\,s^{-1}}$ and 4 μas as appropriate to ground-based RV studies and for *SIM*. In both cases, we assumed 250 observations spread over 10 yr and required a final signal-to-noise ratio of 5.8 relative to the amplitude of the reflex motion (Traub et al. 2009). For planet periods greater than the observational duration, we degraded the noise performance according to $(\mathrm{period}/10\ \mathrm{yr})^3$. To account for photospheric variability, rotation, and other deleterious effects, we parameterized the stellar RV and astrometric jitter between 1 Myr and 5 Gyr as power laws between $100\ \mathrm{m\,s^{-1}}$ and $1\ \mathrm{s^{-1}}$ and $4 \times (140\ \mathrm{pc/Dist})$ μas to $1 \times (140\ \mathrm{pc/Dist})$ μas (Makarov et al. 2009). Radial velocity measurements were not considered for stellar types earlier than F0 due to the difficulty of finding suitable spectral lines.

Columns (11) and (12) of Table 5 and Table 6 give the fraction of planets detected by imaging that might also be detected via RV or astrometric measurements. The most favorable systems are those found at the smallest separations, i.e., those imaged using TFI/NRM, MIRI/FQPM, or TMT. Up to 30% of TMT imaging detections could, in the most favorable cases, also be detected via *SIM* astrometry. The majority of the mass measurements will have to be obtained with precision astrometry, because of the competing selection effects of improved imaging and astrometric detectability with orbital radius on the one hand, and of decreasing RV amplitude with increasing radius on the other.

Precise mass measurements will not be possible for the planets located at 10 s of AU from their host stars. While the absolute astrometric shifts are large (hundreds of μas), the orbital time scales (tens to hundreds of years) are too long to cover a significant portion of an orbit during *SIM*'s mission lifetime. However, measurements of orbital accelerations over a 5–10 yr baseline can give a useful indicator of planet mass. While the linear terms of the stellar reflex motion are absorbed into the host's proper motion, the first (quadratic) term in the deviation from stellar proper motion due a long period orbit is given approximately by

$$\text{Nonlinear deviation} \sim \frac{2\pi^2 \mathrm{A}}{\text{Dist}} \frac{a_{\mathrm{Jup}}^2}{a^2} \frac{M_{\mathrm{p}}}{M_{\mathrm{Jup}}} t_{\mathrm{obs}}^2$$
$$= 7.6 \frac{25 \text{ pc}}{\text{Dist}} \frac{M_{\mathrm{p}}}{M_{\mathrm{Jup}}} \left(\frac{50 \text{ AU}}{a}\right)^2 \left(\frac{t_{\mathrm{obs}}}{5 \text{ yr}}\right)^2 \mu\text{as}, \qquad (3)$$

where $\mathrm{A} = 500$ μas, a is the semimajor axis, and $t_{\mathrm{obs}} \ll T_{\mathrm{Period}}$ is the measurement duration, or roughly 38 μas for a 5 M_{Jup} planet in a 50 AU orbit at 25 pc. This deviation from stellar proper motion and parallax would be detectable by *SIM* Lite. The interpretation of the measurements would be complicated by the unknown eccentricity and orientation, but the results would help to constrain the masses of distant planets detected with imaging, particularly in the absence of a visible dust disk. A full discussion of recovery of planet parameters from incomplete orbits is beyond the scope of this article. The reader is referred to Traub et al (2009) for more information.

7. CONCLUSIONS

This article has combined estimates of the performance of a number of instruments, evolutionary tracks of planets, and possible populations of planets to assess the potential for the direct detection of planets using high-contrast imaging. The results are necessarily speculative given the considerable uncertainties in each area: projections of instrument and telescope performance tend to be optimistic, some of the fundamental physics underlying the evolutionary tracks remains in question, and the number of planets on distant orbits and the mechanisms for getting them there are largely unknown. Nevertheless, we can draw some robust conclusions from this analysis:

1. The early successes of imaging of planets around HR 8799 and Fomalhaut are harbingers of many results to come. Our Monte Carlo results confirm other predictions that coronagraphs with extreme adaptive optics and postcoronagraph wavefront control, e.g., P1640, GPI, and SPHERE, will be able to detect young planets with average masses of 5 M_{Jup} within <50 AU of young stars and, in favorable cases, find planets as close in as 5–10 AU and with masses as small 1–2 M_{Jup}. The requirement for extreme AO systems to have bright host stars will limit these searches to closer stars and earlier spectral types. The success rates for these instruments will improve with the technology, from 15% for the current generation (NICI, et alia) to 30% for the next generation (P1640, GPI, SPHERE), and perhaps 70% for an optimized TMT instrument. These results depend, of course, on our assumptions of instrument and planet properties. At longer wavelengths, 3–5 μm, ground-based telescopes like the MMT and LBT will similarly be able to detect ~5 M_{Jup} planets with the intrinsic planetary brightness offsetting the higher thermal background at these wavelengths.

2. The Monte Carlo results show that *JWST*'s NIRCam coronagraph can find planets with an average mass of 1.5 M_{Jup} at separations of ~80 AU with masses of a few tenths of a Jupiter mass and separations of 50 AU possible in the most favorable cases. The TFI's nonredundant mask imager will probe a comparable mass range in the inner portions of young stars in the regions like Taurus, while MIRI's four-quadrant phase mask coronagraph will complement NIRCam and TFI/NRM over a broad range of planet masses and separation yielding information on planet radius and temperature. The performance of these instruments depends critically on *JWST* meeting its performance goals (wavefront error, etc.) and are of necessity speculative until the telescope is on orbit. However, these results will be of interest to those planning various instrument campaigns.

3. *JWST*'s sensitivity will allow it to search for 1–2 M_{Jup} objects orbiting nearby M stars (<2 Gyr) at orbits of a few to a few tens of AU. The intrinsic faintness of these few Gyr old objects will make this a very challenging experiment for ground-based telescopes operating at 1–2 μm, particularly given the faintness of many of their host stars and the demands of extreme AO imaging.

4. An extreme AO coronagraph operating at 1.65 μm on a 30–40 m telescope could find ~1 M_{Jup} planets within <5 AU of young parent stars, as well as provide high spectral observations in the near-IR for objects initially detected by *JWST* at longer wavelengths.

5. In addition to studying the physical conditions of these planets, there is a special premium for discovery and characterization of the closest-in systems using *JWST*/NRM, MIRI, and TMT since these objects might also be detected by dynamical techniques using RV, or astrometry with ground-based interferometers GAIA or *SIM* Lite. Combined imaging and dynamical data will anchor evolutionary models of young planets and thereby help to put models for the formation and subsequent evolution of planets on a more sound theoretical footing.

This work used archive information drawn from the NSTeD, 2MASS, and SIMBAD archives. Some of the research described in this publication was carried out at the Jet Propulsion Laboratory, California Institute of Technology, under a contract with the National Aeronautics and Space Administration. The work of A. Sivaramakrishnan is supported in part by the National Science Foundation grant AST-0804417. We gratefully acknowledge I. Baraffe in extending the CONDO3 models to lower masses. C. A. B. is extremely grateful to Ben Oppenheimer, Dave Latham, and Dimitar Sasselov for their hospitality during sabbatical sojourns at the American Museum of Natural History and the Center for Astrophysics. We thank Peter Lawson for providing Figure 1 and Dr. Sally Dodson-Robinson for useful discussions. Finally, we acknowledge the extensive efforts of an anonymous referee whose careful reading and numerous suggestions greatly improved the content and presentation of this article.

APPENDIX A

BROADBAND COLORS FOR PLANETS

Tables 10–19 list absolute magnitudes (10 pc) for planets as observed through standard ground-based filters (J, H, K, L, M), four *JWST*/NIRCAM broadband filters, and three *JWST*/MIRI narrowband filters; one table each for selected ages ranging from 1 Myr to 10 Gyr. For the NIRCam filters we have used measured transmission curves, while for the MIRI filters we have taken a square ($R = 20$) passband centered on 10.65, 11.4, and 15.5 μm as a reasonable approximation for these narrowband filters. The evolutionary tracks represent an extension of CONDO3 models (Baraffe et al. 2003) for planetary masses down to $0.1\ M_{\rm Jup}$ and for ages up to 10 Gyr. Tracks are dropped as the effective temperature for a given mass-age combination drops below 100 K, at which point the model atmosphere calculations become unreliable. The synthetic spectra utilize an updated grid (the GAIA grid) which includes minor corrections to the older "AMES" spectra. The changes to the colors are modest and are too small to impact the cooling tracks in any noticeable way.

APPENDIX B

SELECTED SAMPLES OF STARS

Tables 20–23 present information on the stars with highest fraction of Monte Carlo runs resulting in a detected planet. Up to 25 stars are presented for each instrument configuration. The columns include: (1)–(5) characterize the spectral type, distance, age (Myr), and H magnitude (typically from 2MASS) of the star; (6) and (7) give the average mass of the detected planets; and (8) gives the fraction of runs on which a planet was detected. Columns (8)–(16) repeat this information for a different instrument.

TABLE 10
CALCULATED PLANET MAGNITUDES (10 PC) FOR 1 MYR

M_{pl} ($M_\odot$)	T_{eff} (K)	L_{pl} ($L_\odot$)	log(g) (cgs)	J (mag)	H (mag)	K (mag)	L (mag)	M (mag)	F150W (mag)	F277W (mag)	F356W (mag)	F444W (mag)	MIRI-1 (mag)	MIRI-2 (mag)	MIRI-3 (mag)
0.0001	247	−7.201	2.15	28.26	26.07	35.45	18.83	17.08	23.1	21.58	18.76	15.86	14.66	13.04	12.59
0.0002	384	−6.184	2.2	20.55	19.87	23.05	15.34	14.14	20.67	19.72	16.97	14.25	13.21	11.73	11.32
0.0003	450	−5.9	2.37	19.11	18.57	20.41	14.57	13.49	18.56	18.55	15.76	13.27	12.45	11.06	10.78
0.0004	517	−5.68	2.52	17.87	17.49	18.33	13.93	12.97	17.74	18.32	15.38	13.01	12.33	10.9	10.67
0.0005	628	−5.37	2.64	16.55	16.28	16.43	13.15	12.45	16.73	17.29	14.51	12.42	11.41	10.33	10.17
0.001	942	−4.715	3	14.52	14.11	13.69	11.52	11.45	14.77	14.67	12.49	11.2	9.84	9.47	9.45
0.002	1285	−4.137	3.26	12.87	12.38	11.95	10.27	10.64	13.13	12.58	10.87	10.28	9.07	8.96	8.98
0.003	1553	−3.746	3.37	11.81	11.36	10.89	9.57	10.09	12.1	11.59	9.95	9.67	8.68	8.62	8.62
0.004	1747	−3.482	3.44	11.12	10.71	10.21	9.12	9.66	11.41	10.93	9.41	9.23	8.39	8.36	8.35
0.005	1901	−3.273	3.47	10.6	10.22	9.73	8.77	9.28	10.84	10.36	9	8.85	8.13	8.1	8.1
0.006	2004	−3.129	3.5	10.23	9.87	9.4	8.52	8.97	10.43	9.93	8.72	8.56	7.92	7.9	7.9
0.007	2098	−2.998	3.52	9.91	9.55	9.11	8.29	8.69	10.06	9.52	8.45	8.29	7.72	7.7	7.7
0.008	2159	−2.893	3.52	9.67	9.3	8.87	8.08	8.45	9.78	9.22	8.23	8.06	7.53	7.52	7.51
0.009	2207	−2.811	3.53	9.48	9.11	8.68	7.92	8.26	9.56	8.99	8.06	7.89	7.39	7.37	7.37
0.010	2251	−2.735	3.53	9.3	8.93	8.52	7.78	8.09	9.36	8.77	7.9	7.72	7.25	7.23	7.22
0.012	2321	−2.615	3.54	9.02	8.65	8.25	7.54	7.81	9.05	8.43	7.65	7.46	7.04	7.02	7.01
0.015	2400	−2.455	3.54	8.64	8.27	7.89	7.21	7.45	8.64	8	7.31	7.12	6.72	6.71	6.69
0.020	2484	−2.28	3.55	8.22	7.86	7.49	6.85	7.05	8.19	7.54	6.92	6.73	6.37	6.36	6.34
0.030	2598	−2.174	3.69	8	7.62	7.27	6.68	6.85	7.91	7.29	6.74	6.55	6.23	6.22	6.2
0.040	2746	−1.939	3.68	7.5	7.1	6.76	6.22	6.31	7.33	6.73	6.26	6.08	5.8	5.79	5.77
0.050	2768	−1.637	3.49	6.74	6.35	6.02	5.48	5.57	6.58	5.98	5.52	5.34	5.07	5.05	5.03
0.060	2824	−1.604	3.57	6.68	6.28	5.96	5.44	5.52	6.49	5.92	5.48	5.3	5.04	5.03	5.01
0.070	2853	−1.478	3.53	6.37	5.96	5.65	5.15	5.23	6.17	5.61	5.18	5.01	4.76	4.74	4.72
0.072	2858	−1.455	3.52	6.31	5.9	5.6	5.1	5.18	6.11	5.56	5.13	4.95	4.71	4.69	4.67
0.075	2833	−1.389	3.46	6.14	5.73	5.42	4.91	5	5.95	5.38	4.95	4.77	4.51	4.5	4.47
0.080	2869	−1.373	3.49	6.11	5.7	5.4	4.9	4.98	5.91	5.36	4.93	4.76	4.51	4.5	4.48
0.090	2867	−1.289	3.46	5.89	5.48	5.18	4.69	4.77	5.7	5.15	4.72	4.55	4.3	4.29	4.26
0.100	2856	−1.187	3.39	5.63	5.22	4.92	4.43	4.51	5.44	4.89	4.46	4.28	4.04	4.02	4

NOTE.—Assumed central wavelengths for the MIRI/FQPM narrowband filters are 10.65, 11.4, and 15.5 μm with a simple square passband with resolution of 20.

TABLE 11

CALCULATED PLANET MAGNITUDES (10 PC) FOR 5 MYR

M_{pl} ($M_\odot$)	T_{eff} (K)	L_{pl} ($L_\odot$)	log(g) (cgs)	J (mag)	H (mag)	K (mag)	L (mag)	M (mag)	F150W (mag)	F277W (mag)	F356W (mag)	F444W (mag)	MIRI-1 (mag)	MIRI-2 (mag)	MIRI-3 (mag)
0.0001	217	−7.514	2.24	31.39	28.37	39.89	20.08	18.13	23.72	22.08	19.24	16.31	15.07	13.43	12.97
0.0002	308	−6.769	2.41	22.75	22.04	27.36	16.77	15.38	22.18	20.92	18.13	15.31	14.18	12.63	12.2
0.0003	360	−6.46	2.55	21.47	20.8	24.72	16.05	14.78	21.39	20.34	17.58	14.83	13.77	12.27	11.85
0.0004	400	−6.284	2.68	20.51	19.9	22.81	15.58	14.39	19.66	19.1	16.5	13.91	12.94	11.65	11.34
0.0005	455	−6.079	2.79	19.37	18.91	20.96	15.03	13.92	18.91	19.01	16.26	13.74	13.03	11.62	11.34
0.001	644	−5.522	3.14	16.84	16.57	16.97	13.56	12.85	16.98	17.6	14.92	12.79	11.92	10.85	10.67
0.002	901	−4.92	3.42	14.94	14.66	14.3	12.07	11.83	15.31	15.42	13.18	11.68	10.46	9.94	9.88
0.003	1098	−4.552	3.58	13.89	13.56	13.21	11.21	11.31	14.23	13.96	12.06	11.03	9.74	9.52	9.51
0.004	1263	−4.283	3.67	13.16	12.79	12.46	10.66	10.96	13.48	13.05	11.33	10.62	9.42	9.29	9.28
0.005	1413	−4.061	3.74	12.58	12.17	11.85	10.23	10.67	12.9	12.39	10.71	10.27	9.18	9.1	9.09
0.006	1543	−3.886	3.8	12.11	11.72	11.36	9.92	10.44	12.43	12.01	10.36	10.01	9.02	8.96	8.93
0.007	1668	−3.725	3.84	11.69	11.3	10.9	9.64	10.2	12.02	11.61	10.01	9.76	8.86	8.82	8.79
0.008	1786	−3.579	3.87	11.33	10.95	10.52	9.4	9.97	11.63	11.24	9.71	9.53	8.71	8.68	8.66
0.009	1885	−3.46	3.9	11.04	10.68	10.24	9.22	9.76	11.32	10.94	9.49	9.34	8.58	8.56	8.54
0.01	1965	−3.363	3.92	10.8	10.44	10	9.06	9.57	11.04	10.64	9.3	9.15	8.46	8.44	8.43
0.012	2102	−3.194	3.95	10.39	10.03	9.61	8.77	9.21	10.55	10.11	8.96	8.81	8.23	8.22	8.21
0.015	2264	−2.981	3.96	9.92	9.53	9.14	8.39	8.72	9.96	9.45	8.53	8.37	7.9	7.88	7.87
0.020	2452	−2.661	3.9	9.18	8.79	8.42	7.77	8	9.13	8.55	7.86	7.68	7.31	7.29	7.28
0.030	2616	−2.262	3.8	8.23	7.85	7.5	6.91	7.07	8.13	7.52	6.97	6.79	6.48	6.46	6.44
0.040	2754	−2.068	3.81	7.82	7.42	7.08	6.54	6.63	7.65	7.06	6.59	6.41	6.13	6.12	6.1
0.050	2806	−1.846	3.72	7.28	6.88	6.55	6.03	6.11	7.1	6.52	6.07	5.9	5.63	5.62	5.59
0.060	2875	−1.902	3.9	7.45	7.03	6.72	6.22	6.3	7.23	6.68	6.26	6.09	5.84	5.83	5.81
0.070	2916	−1.829	3.92	7.28	6.85	6.55	6.07	6.14	7.04	6.51	6.1	5.94	5.7	5.69	5.67
0.072	2921	−1.814	3.92	7.24	6.82	6.51	6.03	6.11	7	6.48	6.06	5.9	5.67	5.65	5.63
0.075	2912	−1.716	3.83	6.99	6.57	6.27	5.78	5.86	6.76	6.23	5.81	5.65	5.41	5.4	5.38
0.080	2946	−1.76	3.92	7.11	6.68	6.39	5.92	6	6.87	6.35	5.94	5.79	5.56	5.55	5.53
0.090	2974	−1.696	3.93	6.96	6.53	6.24	5.78	5.85	6.7	6.2	5.79	5.64	5.42	5.41	5.39
0.100	2983	−1.582	3.87	6.67	6.24	5.95	5.5	5.58	6.42	5.92	5.52	5.37	5.15	5.14	5.12

NOTE.—Assumed central wavelengths for the MIRI/FQPM narrowband filters are 10.65, 11.4, and 15.5 μm with a simple square passband with resolution of 20.

TABLE 12

CALCULATED PLANET MAGNITUDES (10 PC) FOR 10 MYR

M_{pl} ($M_\odot$)	T_{eff} (K)	L_{pl} ($L_\odot$)	log(g) (cgs)	J (mag)	H (mag)	K (mag)	L (mag)	M (mag)	F150W (mag)	F277W (mag)	F356W (mag)	F444W (mag)	MIRI-1 (mag)	MIRI-2 (mag)	MIRI-3 (mag)
0.0001	196	−7.739	2.29	33.53	29.94	42.93	20.92	18.84	24.12	22.39	19.55	16.59	15.32	13.66	13.19
0.0002	274	−7.048	2.49	25.63	24.2	31.59	17.95	16.38	22.82	21.41	18.61	15.74	14.58	12.99	12.54
0.0003	326	−6.713	2.62	22.36	21.75	26.77	16.68	15.3	22.01	20.8	18.05	15.26	14.17	12.64	12.21
0.0004	366	−6.499	2.74	21.36	20.8	24.78	16.16	14.87	21.44	20.41	17.68	14.95	13.92	12.44	12.01
0.0005	394	−6.38	2.85	20.7	20.16	23.4	15.83	14.61	21.07	20.16	17.45	14.76	13.76	12.32	11.91
0.001	540	−5.87	3.18	18.12	17.79	19.05	14.48	13.5	18.02	18.67	15.91	13.51	13	11.61	11.34
0.002	746	−5.298	3.47	16.02	15.79	15.86	13.02	12.47	16.29	16.77	14.29	12.36	11.35	10.53	10.39
0.003	920	−4.914	3.63	14.88	14.65	14.33	12.09	11.84	15.26	15.35	13.17	11.67	10.48	9.98	9.92
0.004	1064	−4.645	3.74	14.12	13.85	13.51	11.46	11.45	14.5	14.33	12.37	11.21	9.97	9.68	9.65
0.005	1193	−4.429	3.82	13.52	13.22	12.92	10.99	11.18	13.88	13.52	11.75	10.87	9.66	9.48	9.47
0.006	1316	−4.244	3.88	13.03	12.68	12.41	10.62	10.95	13.35	12.93	11.25	10.59	9.44	9.32	9.3
0.007	1426	−4.091	3.94	12.64	12.27	11.99	10.33	10.77	12.94	12.51	10.85	10.36	9.3	9.21	9.17
0.008	1536	−3.945	3.98	12.25	11.87	11.56	10.07	10.58	12.57	12.17	10.53	10.15	9.16	9.09	9.05
0.009	1635	−3.82	4.01	11.92	11.54	11.19	9.84	10.4	12.26	11.88	10.26	9.97	9.04	8.99	8.95
0.010	1731	−3.704	4.04	11.63	11.26	10.87	9.65	10.23	11.94	11.57	10	9.78	8.92	8.89	8.85
0.012	1915	−3.488	4.08	11.1	10.75	10.33	9.32	9.87	11.38	11.02	9.59	9.44	8.71	8.68	8.66
0.015	2188	−3.125	4.05	10.25	9.87	9.47	8.68	9.07	10.33	9.88	8.85	8.69	8.17	8.16	8.15
0.020	2442	−2.709	3.94	9.3	8.91	8.54	7.88	8.11	9.25	8.68	7.98	7.8	7.42	7.41	7.39
0.030	2622	−2.435	3.97	8.68	8.28	7.93	7.35	7.5	8.56	7.97	7.41	7.24	6.92	6.91	6.89
0.040	2734	−2.411	4.14	8.67	8.25	7.92	7.37	7.5	8.5	7.93	7.43	7.26	6.98	6.97	6.95
0.050	2821	−2.233	4.12	8.26	7.84	7.52	7	7.1	8.06	7.5	7.05	6.88	6.62	6.61	6.59
0.060	2871	−2.188	4.18	8.16	7.73	7.43	6.93	7.03	7.94	7.41	6.97	6.81	6.56	6.55	6.53
0.070	2919	−2.099	4.19	7.95	7.52	7.22	6.74	6.83	7.71	7.19	6.77	6.62	6.38	6.37	6.35
0.072	2927	−2.083	4.19	7.91	7.48	7.18	6.7	6.8	7.67	7.15	6.74	6.58	6.35	6.33	6.31
0.075	2942	−2.022	4.16	7.76	7.33	7.04	6.56	6.65	7.52	7.01	6.59	6.44	6.21	6.2	6.18
0.080	2958	−2.016	4.19	7.75	7.32	7.03	6.56	6.65	7.51	7	6.59	6.44	6.21	6.2	6.18
0.090	2993	−1.943	4.19	7.58	7.14	6.86	6.41	6.49	7.32	6.83	6.42	6.28	6.06	6.05	6.03
0.100	3024	−1.854	4.16	7.37	6.93	6.65	6.21	6.29	7.1	6.61	6.22	6.08	5.87	5.86	5.84

NOTE.—Assumed central wavelengths for the MIRI/FQPM narrow band filters are 10.65, 11.4, and 15.5 μm with a simple square passband with resolution of 20.

TABLE 13

CALCULATED PLANET MAGNITUDES (10 PC) FOR 50 MYR

$M_{\rm pl}$ ($M_\odot$)	$T_{\rm eff}$ (K)	$L_{\rm pl}$ ($L_\odot$)	log(g) (cgs)	J (mag)	H (mag)	K (mag)	L (mag)	M (mag)	F150W (mag)	F277W (mag)	F356W (mag)	F444W (mag)	MIRI-1 (mag)	MIRI-2 (mag)	MIRI-3 (mag)
0.0001	139	−8.453	2.41	39.4	34.24	51.32	23.18	20.73	25.17	23.2	20.33	17.29	15.96	14.24	13.76
0.0002	196	−7.794	2.65	33.33	29.9	43.33	21.08	18.97	24.22	22.42	19.65	16.7	15.47	13.8	13.32
0.0003	232	−7.465	2.79	29.54	27.25	38.39	19.78	17.86	23.62	21.92	19.23	16.32	15.17	13.54	13.06
0.0004	262	−7.232	2.89	26.54	25.17	34.3	18.72	16.95	23.14	21.56	18.9	16.04	14.94	13.34	12.87
0.0005	285	−7.069	2.97	24.23	23.59	31.08	17.89	16.24	22.81	21.32	18.68	15.85	14.78	13.21	12.75
0.001	375	−6.587	3.27	21.1	20.8	25.14	16.44	15.02	21.51	20.45	17.88	15.16	14.25	12.77	12.35
0.002	491	−6.1	3.55	18.92	18.55	20.7	15.15	13.94	18.68	19.17	16.51	13.97	13.64	12.2	11.83
0.003	585	−5.789	3.72	17.63	17.39	18.67	14.31	13.34	17.68	18.3	15.75	13.36	12.86	11.62	11.34
0.004	676	−5.531	3.84	16.72	16.51	17.21	13.64	12.85	16.91	17.45	15.01	12.82	12.09	11.09	10.88
0.005	756	−5.336	3.93	16.09	15.91	16.2	13.16	12.51	16.37	16.77	14.44	12.44	11.55	10.74	10.58
0.006	840	−5.152	4.01	15.51	15.36	15.34	12.72	12.21	15.88	16.12	13.91	12.11	11.11	10.45	10.33
0.007	928	−4.978	4.08	14.98	14.85	14.64	12.31	11.94	15.4	15.48	13.39	11.8	10.71	10.19	10.11
0.008	1010	−4.832	4.14	14.55	14.41	14.14	11.97	11.74	14.99	14.94	12.96	11.55	10.42	10.02	9.96
0.009	1085	−4.706	4.19	14.19	14.04	13.76	11.69	11.59	14.63	14.48	12.59	11.36	10.21	9.9	9.86
0.010	1171	−4.569	4.23	13.82	13.64	13.38	11.38	11.43	14.26	13.99	12.21	11.17	10.02	9.8	9.77
0.012	1520	−4.052	4.24	12.49	12.17	11.95	10.34	10.81	12.83	12.45	10.82	10.39	9.41	9.33	9.28
0.015	1903	−3.568	4.25	11.29	10.94	10.56	9.5	10.06	11.57	11.24	9.77	9.62	8.88	8.86	8.82
0.020	1909	−3.642	4.45	11.47	11.13	10.79	9.69	10.26	11.74	11.45	9.97	9.82	9.08	9.06	9.02
0.030	2246	−3.311	4.58	10.7	10.33	9.98	9.19	9.63	10.77	10.44	9.36	9.23	8.72	8.71	8.69
0.040	2480	−3.08	4.64	10.21	9.81	9.48	8.82	9.12	10.14	9.72	8.93	8.78	8.41	8.4	8.38
0.050	2651	−2.884	4.66	9.79	9.38	9.06	8.48	8.7	9.64	9.18	8.56	8.4	8.1	8.09	8.07
0.060	2759	−2.755	4.68	9.51	9.09	8.79	8.24	8.42	9.34	8.86	8.32	8.16	7.89	7.88	7.86
0.070	2837	−2.647	4.69	9.27	8.84	8.55	8.04	8.19	9.08	8.6	8.1	7.95	7.69	7.68	7.67
0.072	2852	−2.623	4.68	9.22	8.79	8.5	7.99	8.14	9.01	8.53	8.04	7.89	7.64	7.63	7.61
0.075	2872	−2.591	4.68	9.15	8.71	8.42	7.92	8.07	8.93	8.45	7.98	7.83	7.58	7.57	7.56
0.080	2901	−2.551	4.69	9.06	8.62	8.34	7.85	7.99	8.82	8.34	7.89	7.74	7.5	7.49	7.47
0.090	2948	−2.472	4.69	8.88	8.44	8.16	7.68	7.82	8.63	8.15	7.72	7.57	7.35	7.34	7.32
0.100	2989	−2.397	4.68	8.7	8.26	7.99	7.53	7.65	8.45	7.98	7.56	7.42	7.2	7.19	7.18

NOTE.—Assumed central wavelengths for the MIRI/FQPM narrow band filters are 10.65, 11.4, and 15.5 μm with a simple square passband with resolution of 20.

TABLE 14

Calculated Planet Magnitudes (10 pc) For 100 Myr

M_{pl} ($M_\odot$)	T_{eff} (K)	L_{pl} ($L_\odot$)	log(g) (cgs)	J (mag)	H (mag)	K (mag)	L (mag)	M (mag)	F150W (mag)	F277W (mag)	F356W (mag)	F444W (mag)	MIRI-1 (mag)	MIRI-2 (mag)	MIRI-3 (mag)
0.0001	115	−8.816	2.45	41.81	35.99	54.78	24.1	21.49	25.57	23.5	20.62	17.55	16.2	14.45	13.96
0.0002	160	−8.188	2.69	36.66	32.33	48.49	22.42	20.08	24.8	22.81	20.07	17.07	15.82	14.11	13.61
0.0003	190	−7.858	2.84	33.38	30.03	44.4	21.32	19.15	24.29	22.37	19.7	16.75	15.57	13.89	13.39
0.0004	218	−7.599	2.94	30.57	28.07	40.63	20.34	18.3	23.82	21.99	19.37	16.46	15.33	13.68	13.18
0.0005	240	−7.418	3.02	28.42	26.59	37.66	19.57	17.64	23.5	21.75	19.16	16.27	15.18	13.56	13.06
0.001	309	−6.957	3.3	22.43	22.38	29.11	17.41	15.69	22.47	21.03	18.51	15.71	14.76	13.19	12.73
0.002	425	−6.383	3.58	20.05	19.76	23.13	15.94	14.55	19.62	19.3	16.89	14.28	13.67	12.31	11.98
0.003	493	−6.112	3.75	18.88	18.57	20.88	15.21	13.93	18.71	19.12	16.58	14.01	13.71	12.3	11.92
0.004	563	−5.88	3.87	17.95	17.71	19.35	14.59	13.5	17.96	18.49	16.02	13.56	13.15	11.87	11.55
0.005	630	−5.686	3.96	17.23	17.02	18.15	14.06	13.14	17.34	17.89	15.48	13.15	12.58	11.46	11.2
0.006	688	−5.534	4.05	16.71	16.51	17.26	13.67	12.83	16.91	17.36	15.02	12.82	12.1	11.15	10.94
0.007	760	−5.365	4.12	16.16	16.01	16.38	13.26	12.55	16.45	16.76	14.52	12.5	11.64	10.84	10.68
0.008	816	−5.246	4.18	15.76	15.65	15.79	12.97	12.35	16.13	16.34	14.17	12.28	11.35	10.66	10.52
0.009	886	−5.103	4.23	15.32	15.23	15.16	12.63	12.13	15.74	15.85	13.77	12.04	11.04	10.45	10.34
0.010	953	−4.978	4.28	14.94	14.86	14.69	12.34	11.96	15.4	15.42	13.41	11.83	10.78	10.29	10.2
0.012	1335	−4.332	4.3	13.2	12.97	12.76	10.9	11.17	13.58	13.19	11.55	10.82	9.74	9.6	9.56
0.015	1399	−4.281	4.42	13.05	12.82	12.65	10.83	11.15	13.44	13.05	11.44	10.8	9.75	9.64	9.58
0.020	1561	−4.11	4.57	12.6	12.34	12.17	10.53	10.99	12.95	12.6	11.01	10.57	9.63	9.56	9.49
0.030	1979	−3.668	4.72	11.52	11.2	10.9	9.82	10.38	11.77	11.5	10.07	9.93	9.24	9.22	9.18
0.040	2270	−3.386	4.8	10.89	10.52	10.19	9.39	9.84	10.95	10.65	9.56	9.44	8.94	8.93	8.9
0.050	2493	−3.167	4.84	10.43	10.02	9.71	9.04	9.37	10.35	9.98	9.17	9.03	8.65	8.64	8.62
0.060	2648	−3.008	4.86	10.1	9.68	9.37	8.78	9.03	9.95	9.54	8.87	8.73	8.42	8.41	8.39
0.070	2762	−2.879	4.87	9.82	9.39	9.1	8.55	8.75	9.65	9.21	8.64	8.49	8.21	8.2	8.19
0.072	2782	−2.856	4.88	9.77	9.34	9.05	8.51	8.7	9.6	9.16	8.6	8.45	8.18	8.17	8.15
0.075	2809	−2.821	4.88	9.69	9.26	8.97	8.44	8.63	9.51	9.07	8.52	8.37	8.11	8.1	8.08
0.080	2846	−2.776	4.88	9.6	9.16	8.87	8.36	8.53	9.39	8.95	8.43	8.28	8.03	8.02	8
0.090	2910	−2.689	4.88	9.4	8.96	8.68	8.19	8.35	9.16	8.7	8.24	8.09	7.86	7.85	7.83
0.100	2960	−2.617	4.89	9.24	8.8	8.52	8.05	8.19	8.98	8.53	8.09	7.94	7.72	7.71	7.7

Note.—Assumed central wavelengths for the MIRI/FQPM narrow band filters are 10.65, 11.4, and 15.5 μm with a simple square passband with resolution of 20.

TABLE 15

Calculated Planet Magnitudes (10 pc) For 120 Myr

M_{pl} ($M_\odot$)	T_{eff} (K)	L_{pl} ($L_\odot$)	log(g) (cgs)	J (mag)	H (mag)	K (mag)	L (mag)	M (mag)	F150W (mag)	F277W (mag)	F356W (mag)	F444W (mag)	MIRI-1 (mag)	MIRI-2 (mag)	MIRI-3 (mag)
0.0001	109	−8.919	2.46	42.43	36.44	55.66	24.33	21.69	25.67	23.58	20.69	17.62	16.25	14.5	14.01
0.0002	152	−8.294	2.71	37.47	32.91	49.74	22.74	20.35	24.92	22.89	20.15	17.14	15.89	14.17	13.67
0.0003	179	−7.971	2.85	34.38	30.75	45.96	21.72	19.48	24.45	22.47	19.81	16.84	15.66	13.96	13.46
0.0004	205	−7.719	2.95	31.76	28.92	42.51	20.81	18.7	24.03	22.12	19.51	16.59	15.45	13.78	13.28
0.0005	227	−7.526	3.03	29.59	27.43	39.5	20.03	18.03	23.68	21.87	19.28	16.38	15.29	13.64	13.14
0.001	295	−7.043	3.31	23.06	22.92	30.33	17.71	15.92	22.68	21.16	18.64	15.83	14.87	13.28	12.81
0.002	403	−6.481	3.59	20.41	20.14	23.91	16.18	14.75	19.93	19.34	17.01	14.38	13.68	12.34	12.02
0.003	475	−6.183	3.75	19.17	18.88	21.55	15.42	14.09	18.97	19.16	16.68	14.1	13.72	12.33	11.95
0.004	537	−5.97	3.88	18.29	18.03	19.95	14.84	13.66	18.25	18.72	16.25	13.75	13.4	12.07	11.72
0.005	599	−5.781	3.97	17.53	17.32	18.69	14.3	13.31	17.6	18.17	15.76	13.35	12.87	11.67	11.38
0.006	665	−5.602	4.05	16.94	16.75	17.67	13.85	12.97	17.11	17.57	15.23	12.98	12.32	11.31	11.07
0.007	716	−5.477	4.13	16.51	16.35	16.95	13.53	12.73	16.74	17.11	14.84	12.7	11.93	11.04	10.85
0.008	783	−5.326	4.19	16.02	15.9	16.18	13.17	12.48	16.34	16.59	14.4	12.43	11.55	10.8	10.64
0.009	835	−5.219	4.24	15.67	15.58	15.68	12.92	12.31	16.05	16.21	14.09	12.23	11.29	10.63	10.49
0.010	900	−5.088	4.29	15.26	15.18	15.09	12.6	12.11	15.69	15.77	13.71	12	11	10.43	10.32
0.012	1273	−4.432	4.31	13.45	13.25	13.03	11.11	11.29	13.86	13.51	11.83	10.99	9.87	9.71	9.68
0.015	1298	−4.436	4.45	13.43	13.27	13.07	11.15	11.34	13.86	13.49	11.85	11.02	9.93	9.77	9.74
0.020	1484	−4.218	4.59	12.87	12.65	12.51	10.75	11.13	13.24	12.87	11.29	10.74	9.76	9.67	9.6
0.030	1905	−3.764	4.74	11.75	11.44	11.17	9.98	10.56	12.02	11.75	10.26	10.1	9.36	9.34	9.29
0.040	2204	−3.472	4.83	11.08	10.72	10.4	9.54	10.03	11.18	10.91	9.73	9.61	9.07	9.06	9.03
0.050	2441	−3.244	4.88	10.6	10.2	9.89	9.19	9.55	10.54	10.2	9.32	9.18	8.78	8.77	8.75
0.060	2606	−3.083	4.91	10.26	9.84	9.54	8.93	9.2	10.13	9.75	9.04	8.9	8.57	8.56	8.54
0.070	2733	−2.944	4.92	9.97	9.54	9.25	8.69	8.91	9.79	9.37	8.77	8.63	8.34	8.33	8.31
0.072	2753	−2.922	4.92	9.92	9.49	9.2	8.65	8.86	9.76	9.33	8.74	8.6	8.32	8.31	8.29
0.075	2783	−2.886	4.92	9.84	9.41	9.12	8.58	8.78	9.67	9.24	8.67	8.52	8.25	8.24	8.22
0.080	2824	−2.838	4.93	9.74	9.3	9.02	8.5	8.68	9.55	9.12	8.57	8.43	8.17	8.16	8.14
0.090	2894	−2.753	4.94	9.56	9.11	8.83	8.34	8.5	9.31	8.87	8.39	8.24	8.01	8	7.98
0.100	2949	−2.673	4.94	9.38	8.93	8.66	8.18	8.33	9.12	8.68	8.23	8.08	7.86	7.85	7.83

Note.—Assumed central wavelengths for the MIRI/FQPM narrow band filters are 10.65, 11.4, and 15.5 μm with a simple square passband with resolution of 20.

TABLE 16
CALCULATED PLANET MAGNITUDES (10 PC) FOR 500 MYR

M_{pl} ($M_\odot$)	T_{eff} (K)	L_{pl} ($L_\odot$)	log(g) (cgs)	J (mag)	H (mag)	K (mag)	L (mag)	M (mag)	F150W (mag)	F277W (mag)	F356W (mag)	F444W (mag)	MIRI-1 (mag)	MIRI-2 (mag)	MIRI-3 (mag)
0.0004	128	−8.602	3.01	38.69	33.88	53.5	23.59	21.03	25.18	22.84	20.3	17.28	16.1	14.33	13.79
0.0005	141	−8.415	3.1	37.42	33.07	51.62	23.09	20.59	24.97	22.66	20.14	17.14	16	14.23	13.69
0.001	203	−7.753	3.37	31.61	29.15	43.23	20.93	18.68	24.04	21.98	19.52	16.61	15.59	13.87	13.35
0.002	272	−7.218	3.64	25.07	24.62	34.02	18.66	16.58	22.99	21.3	18.9	16.04	15.21	13.55	13.05
0.003	322	−6.913	3.81	22.05	22.27	29.03	17.52	15.53	22.27	20.82	18.48	15.65	14.92	13.33	12.85
0.004	370	−6.67	3.93	21.01	21.06	26.45	16.85	15.05	21.62	20.34	18.06	15.28	14.58	13.08	12.62
0.005	409	−6.496	4.03	20.2	20.11	24.54	16.32	14.67	19.97	19.32	17.13	14.46	13.85	12.53	12.16
0.006	449	−6.34	4.11	19.64	19.51	23.1	15.92	14.36	19.48	19.17	16.97	14.31	13.87	12.53	12.15
0.007	488	−6.2	4.18	19.1	18.91	21.68	15.52	14.06	19.04	19.04	16.83	14.19	13.88	12.54	12.14
0.008	525	−6.08	4.25	18.65	18.46	20.74	15.19	13.83	18.68	18.78	16.6	14	13.67	12.38	12
0.009	564	−5.963	4.31	18.21	18.04	19.95	14.88	13.63	18.3	18.44	16.3	13.76	13.37	12.15	11.8
0.010	599	−5.864	4.36	17.8	17.66	19.22	14.59	13.43	17.93	18.13	16	13.52	13.08	11.92	11.61
0.012	759	−5.447	4.43	16.38	16.29	16.82	13.51	12.68	16.7	16.84	14.76	12.67	11.89	11.11	10.92
0.015	791	−5.404	4.56	16.2	16.16	16.58	13.41	12.6	16.56	16.62	14.61	12.58	11.78	11.06	10.88
0.020	936	−5.133	4.7	15.33	15.34	15.37	12.78	12.21	15.82	15.72	13.85	12.14	11.23	10.71	10.58
0.030	1264	−4.636	4.91	13.9	13.87	13.69	11.7	11.68	14.41	14.07	12.48	11.44	10.43	10.22	10.18
0.040	1583	−4.255	5.04	12.92	12.76	12.68	10.95	11.33	13.32	12.96	11.46	10.95	10.06	9.98	9.9
0.050	1875	−3.955	5.13	12.21	11.95	11.79	10.44	10.99	12.49	12.22	10.74	10.53	9.79	9.76	9.69
0.060	2116	−3.729	5.19	11.69	11.36	11.13	10.1	10.63	11.87	11.65	10.32	10.21	9.6	9.58	9.54
0.070	2329	−3.534	5.23	11.27	10.9	10.63	9.81	10.26	11.28	11.04	9.96	9.85	9.37	9.36	9.33
0.072	2369	−3.498	5.24	11.19	10.81	10.54	9.75	10.19	11.18	10.93	9.9	9.78	9.33	9.31	9.29
0.075	2426	−3.445	5.24	11.08	10.69	10.42	9.67	10.08	11.04	10.78	9.82	9.7	9.27	9.26	9.23
0.080	2518	−3.356	5.25	10.89	10.49	10.22	9.53	9.89	10.81	10.52	9.66	9.54	9.16	9.14	9.12
0.090	2680	−3.189	5.24	10.55	10.12	9.85	9.25	9.53	10.37	10.04	9.35	9.22	8.9	8.89	8.88
0.100	2804	−3.047	5.22	10.25	9.8	9.54	9	9.22	10.05	9.68	9.09	8.95	8.68	8.67	8.65

NOTE.—Assumed central wavelengths for the MIRI/FQPM narrow band filters are 10.65, 11.4, and 15.5 μm with a simple square passband with resolution of 20.

TABLE 17

Calculated Planet Magnitudes (10 pc) For 1 Gyr

M_{pl} ($M_{\odot}$)	T_{eff} (K)	L_{pl} ($L_{\odot}$)	log(g) (cgs)	J (mag)	H (mag)	K (mag)	L (mag)	M (mag)	F150W (mag)	F277W (mag)	F356W (mag)	F444W (mag)	MIRI-1 (mag)	MIRI-2 (mag)	MIRI-3 (mag)
0.0005	111	−8.851	3.12	40.19	35.07	55.87	24.15	21.49	25.42	22.94	20.45	17.41	16.26	14.44	13.89
0.001	160	−8.185	3.39	35.58	32.06	49.17	22.4	19.95	24.67	22.36	19.93	16.97	15.93	14.14	13.6
0.002	226	−7.56	3.66	29.28	27.8	40.31	20.18	17.94	23.65	21.73	19.35	16.42	15.58	13.86	13.32
0.003	270	−7.244	3.83	25.29	24.99	34.51	18.84	16.66	22.98	21.3	18.96	16.05	15.33	13.66	13.14
0.004	304	−7.031	3.95	22.49	22.91	30.25	17.91	15.73	22.52	20.98	18.69	15.8	15.14	13.52	13.01
0.005	342	−6.831	4.05	21.71	21.98	28.28	17.38	15.36	22.03	20.61	18.38	15.53	14.91	13.35	12.87
0.006	377	−6.664	4.13	20.96	21.07	26.39	16.87	15.01	21.62	20.27	18.12	15.29	14.68	13.17	12.72
0.007	403	−6.556	4.21	20.41	20.43	25.04	16.54	14.76	20.14	19.32	17.27	14.54	13.98	12.63	12.29
0.008	438	−6.417	4.27	19.93	19.89	23.77	16.18	14.5	19.75	19.2	17.14	14.44	13.98	12.64	12.28
0.009	464	−6.325	4.33	19.59	19.49	22.85	15.93	14.31	19.49	19.11	17.06	14.37	13.98	12.65	12.27
0.010	491	−6.235	4.38	19.23	19.07	21.9	15.65	14.11	19.2	18.99	16.95	14.27	13.94	12.64	12.24
0.012	578	−5.955	4.47	18.15	18.03	19.86	14.88	13.6	18.28	18.3	16.28	13.73	13.33	12.14	11.81
0.015	628	−5.835	4.59	17.7	17.62	19.05	14.56	13.38	17.89	17.88	15.92	13.47	12.97	11.92	11.63
0.020	766	−5.514	4.74	16.56	16.55	17.19	13.72	12.8	16.91	16.83	14.94	12.81	12.08	11.34	11.14
0.030	1009	−5.071	4.95	15.1	15.16	15.14	12.67	12.15	15.64	15.4	13.67	12.07	11.17	10.74	10.62
0.040	1271	−4.696	5.1	14.04	14.04	13.9	11.88	11.8	14.57	14.2	12.66	11.58	10.62	10.41	10.36
0.050	1543	−4.374	5.21	13.21	13.12	13.04	11.25	11.53	13.63	13.24	11.8	11.18	10.29	10.19	10.12
0.060	1801	−4.106	5.29	12.56	12.36	12.27	10.77	11.26	12.87	12.56	11.12	10.82	10.05	10.01	9.94
0.070	2082	−3.829	5.33	11.93	11.62	11.43	10.32	10.85	12.14	11.91	10.56	10.43	9.8	9.78	9.73
0.072	2140	−3.772	5.34	11.8	11.48	11.27	10.23	10.75	11.97	11.75	10.45	10.33	9.74	9.72	9.67
0.075	2234	−3.679	5.33	11.6	11.25	11.02	10.08	10.58	11.66	11.44	10.24	10.14	9.6	9.59	9.55
0.080	2383	−3.527	5.32	11.26	10.89	10.63	9.84	10.27	11.25	11.01	9.98	9.87	9.42	9.41	9.38
0.090	2627	−3.268	5.28	10.72	10.3	10.03	9.4	9.72	10.57	10.27	9.51	9.38	9.05	9.04	9.02
0.100	2784	−3.083	5.25	10.33	9.89	9.62	9.07	9.31	10.13	9.77	9.15	9.02	8.74	8.73	8.71

Note.—Assumed central wavelengths for the MIRI/FQPM narrow band filters are 10.65, 11.4, and 15.5 μm with a simple square passband with resolution of 20.

TABLE 18

CALCULATED PLANET MAGNITUDES (10 PC) FOR 5 GYR

M_{pl} ($M_\odot$)	T_{eff} (K)	L_{pl} ($L_\odot$)	log(g) (cgs)	J (mag)	H (mag)	K (mag)	L (mag)	M (mag)	F150W (mag)	F277W (mag)	F356W (mag)	F444W (mag)	MIRI-1 (mag)	MIRI-2 (mag)	MIRI-3 (mag)
0.002	129	−8.57	3.7	38.16	34.52	53.62	23.33	20.8	25	22.61	20.24	17.19	16.35	14.46	13.86
0.003	162	−8.166	3.87	34.96	32.46	49.21	22.22	19.81	24.49	22.35	20.01	16.94	16.26	14.41	13.79
0.004	193	−7.867	3.99	32.14	30.52	45.15	21.28	18.92	24.04	22.09	19.77	16.71	16.12	14.31	13.7
0.005	220	−7.644	4.09	29.83	28.84	41.71	20.48	18.16	23.47	21.71	19.43	16.42	15.97	14.18	13.57
0.006	244	−7.469	4.18	27.8	27.34	38.67	19.78	17.49	23.06	21.42	19.19	16.22	15.85	14.08	13.48
0.007	265	−7.328	4.25	26.02	26	35.96	19.16	16.88	22.75	21.19	19.02	16.06	15.75	14	13.41
0.008	284	−7.217	4.32	24.5	24.85	33.65	18.64	16.36	22.5	20.99	18.86	15.91	15.63	13.91	13.33
0.009	301	−7.124	4.38	23.21	23.85	31.64	18.18	15.91	22.33	20.83	18.76	15.82	15.54	13.84	13.29
0.010	322	−7.015	4.43	22.74	23.3	30.49	17.91	15.71	22.17	20.68	18.66	15.71	15.42	13.76	13.24
0.012	361	−6.823	4.52	21.77	22.17	28.16	17.41	15.32	21.97	20.41	18.5	15.54	15.16	13.57	13.12
0.015	399	−6.671	4.63	20.85	21.14	26.01	16.96	14.97	21.83	20.15	18.35	15.39	14.9	13.43	13
0.020	473	−6.401	4.79	19.89	19.92	23.31	16.18	14.45	19.87	19.07	17.31	14.56	14.18	12.94	12.53
0.030	610	−6.008	5.01	18.34	18.31	20.04	15.04	13.71	18.48	18.01	16.34	13.82	13.34	12.36	12.02
0.040	760	−5.67	5.18	17.04	17.11	17.99	14.17	13.13	17.38	16.97	15.32	13.17	12.5	11.8	11.57
0.050	931	−5.353	5.31	15.94	16.05	16.38	13.38	12.63	16.41	15.97	14.38	12.6	11.82	11.34	11.17
0.060	1120	−5.058	5.42	15.01	15.13	15.15	12.73	12.27	15.57	15.11	13.6	12.18	11.35	11.02	10.9
0.070	1524	−4.504	5.47	13.52	13.5	13.44	11.6	11.77	13.97	13.56	12.19	11.47	10.6	10.49	10.42
0.072	1712	−4.278	5.45	12.97	12.85	12.8	11.16	11.54	13.33	12.97	11.58	11.15	10.36	10.29	10.21
0.075	2006	−3.942	5.41	12.2	11.92	11.78	10.54	11.06	12.42	12.17	10.78	10.63	9.97	9.94	9.89
0.080	2320	−3.603	5.35	11.44	11.07	10.82	9.97	10.43	11.45	11.22	10.12	10.01	9.52	9.51	9.48
0.090	2622	−3.275	5.29	10.73	10.31	10.04	9.42	9.73	10.58	10.28	9.52	9.39	9.05	9.04	9.02
0.100	2785	−3.083	5.25	10.33	9.89	9.62	9.07	9.31	10.12	9.77	9.15	9.02	8.74	8.73	8.71

NOTE.—Assumed central wavelengths for the MIRI/FQPM narrow band filters are 10.65, 11.4, and 15.5 μm with a simple square passband with resolution of 20.

TABLE 19

CALCULATED PLANET MAGNITUDES (10 PC) FOR 10 GYR

M_{pl} ($M_\odot$)	T_{eff} (K)	L_{pl} ($L_\odot$)	log(g) (cgs)	J (mag)	H (mag)	K (mag)	L (mag)	M (mag)	F150W (mag)	F277W (mag)	F356W (mag)	F444W (mag)	MIRI-1 (mag)	MIRI-2 (mag)	MIRI-3 (mag)
0.003	125	−8.629	3.88	38.29	35.04	54.28	23.36	20.89	24.98	22.7	20.34	17.22	16.56	14.64	13.99
0.004	149	−8.325	4.01	36.01	33.56	51.11	22.59	20.19	24.59	22.49	20.16	17.03	16.49	14.6	13.94
0.005	172	−8.087	4.11	34.06	32.18	48.26	21.92	19.57	24	22.13	19.83	16.76	16.39	14.51	13.84
0.006	193	−7.888	4.2	32.23	30.85	45.53	21.29	18.97	23.56	21.84	19.58	16.55	16.3	14.43	13.76
0.007	213	−7.724	4.27	30.55	29.62	43.01	20.71	18.41	23.18	21.57	19.35	16.36	16.18	14.33	13.67
0.008	232	−7.584	4.34	29	28.46	40.66	20.18	17.89	22.91	21.37	19.19	16.22	16.09	14.26	13.61
0.009	249	−7.469	4.39	27.62	27.41	38.55	19.7	17.42	22.69	21.2	19.07	16.11	16	14.2	13.56
0.01	265	−7.368	4.45	26.34	26.44	36.59	19.26	16.98	22.53	21.06	18.97	16.01	15.93	14.14	13.52
0.012	293	−7.204	4.54	24.04	24.64	33.06	18.48	16.2	22.4	20.86	18.85	15.89	15.74	14.02	13.43
0.015	330	−7.016	4.65	22.7	23.33	30.46	17.93	15.76	22.41	20.65	18.75	15.78	15.46	13.88	13.33
0.020	389	−6.759	4.8	21.28	21.73	27.02	17.21	15.19	22.06	20.24	18.48	15.51	15.07	13.65	13.14
0.030	504	−6.358	5.03	19.72	19.68	22.59	16.04	14.37	19.83	18.96	17.32	14.6	14.2	13.04	12.62
0.040	634	−6.004	5.2	18.33	18.33	19.99	15.03	13.75	18.49	17.9	16.28	13.86	13.33	12.44	12.1
0.050	776	−5.695	5.34	17.1	17.18	18.07	14.23	13.21	17.43	16.94	15.37	13.26	12.59	11.93	11.69
0.060	941	−5.393	5.45	16.04	16.18	16.55	13.5	12.73	16.53	16.01	14.48	12.72	11.96	11.5	11.33
0.070	1289	−4.832	5.5	14.37	14.43	14.36	12.27	12.08	14.89	14.43	13	11.88	11.01	10.8	10.73
0.072	1556	−4.472	5.48	13.44	13.41	13.36	11.55	11.75	13.87	13.46	12.1	11.42	10.57	10.46	10.39
0.075	1997	−3.954	5.41	12.23	11.95	11.81	10.56	11.08	12.44	12.19	10.8	10.64	9.97	9.95	9.89
0.080	2322	−3.602	5.35	11.43	11.06	10.82	9.97	10.43	11.44	11.21	10.12	10.01	9.52	9.51	9.48
0.090	2624	−3.274	5.29	10.73	10.31	10.04	9.41	9.73	10.58	10.28	9.51	9.39	9.05	9.04	9.02
0.100	2786	−3.082	5.25	10.32	9.88	9.62	9.07	9.3	10.12	9.76	9.15	9.02	8.74	8.73	8.71

NOTE.—Assumed central wavelengths for the MIRI/FQPM narrow band filters are 10.65, 11.4, and 15.5 μm with a simple square passband with resolution of 20.

TABLE 20

Young Stars With Highest Probability of Planet Detection

(1) Star	(2) Spec. Type	(3) Dist. (pc)	(4) Log(Age) (yr)	(5) H (mag)	(6) Mass (M_{Jup})	(7) SMA (AU)	(8) Score (%)	(9) Star	(10) Spec. Type	(11) Dist. (pc)	(12) Log(Age) (yr)	(13) H (mag)	(14) Mass (M_{Jup})	(15) SMA (AU)	(16) Score (%)
		P1640/GPI								NIRCam 4.4 μm					
HD 31295 …………	A3V	37.0	7.0	4.4	2.55	29	43	HD 172555	A5 IV/V	29.2	7.1	4.3	1.61	84	40
HD 46190 …………	A0V	79.0	6.7	6.4	2.33	62	42	HD172555	A7	29.2	7.3	4.3	1.96	85	40
HD 110411 …………	A3 Va	36.9	7.0	4.7	2.69	29	42	HD35850	F7	26.8	7.1	5.1	1.39	82	40
HD 172555 …………	A5 IV/V	29.2	7.1	4.3	2.54	23	40	HD164249	F5	23.7	7.3	6.0	1.03	69	40
TWA11A …………	A0	60.0	7.0	5.8	2.91	45	40	HD 39060	A5V	19.3	7.3	3.5	1.74	56	40
BetaPic …………	A3V	19.3	7.3	3.5	2.74	16	40	V383 LAC	K0VIV	33.0	7.8	6.6	1.06	87	39
HD 109573 …………	A0V	67.1	6.9	5.8	2.86	54	40	CD-64d1208	K7	29.2	7.3	6.3	1.03	82	39
HD 146624 …………	A0 (V)	43.1	7.1	4.7	2.67	32	40	HD37572	K0V	23.9	7.8	5.9	1.19	69	38
HD 39060 …………	A5V	19.3	7.3	3.5	2.59	16	38	BetaPic	A3V	19.3	7.3	3.5	1.76	64	38
HD 188228 …………	A0V	32.5	7.0	4.0	2.45	26	38	HD207129	G2	15.6	7.3	4.3	1.24	50	38
HD 183324 …………	A0V	59.0	7.0	5.5	3.30	43	37	51Eri	F0V	29.8	7.3	4.8	1.67	87	38
HD 30422 …………	A3IV	57.5	7.0	5.7	2.82	43	37	HD139813	G5	21.7	8.3	5.6	1.15	67	38
PreibZinn99-67 …….	K5	145.0	6.0	8.7	2.44	74	36	HD17925	K1V	10.4	7.9	4.2	1.16	34	38
HD 38206 …………	A0V	69.2	7.0	5.8	2.95	48	34	HIP23309	M0/1	26.3	7.3	6.4	0.46	82	38
TYC7349-2191-1 …..	K2-IV	130.0	6.0	8.4	2.35	77	32	HD217343	G3V	32.0	7.6	6.0	1.27	94	37
CITau …………	K0?	140.0	5.8	7.7	2.32	81	32	GJ3305	M0.5	29.8	7.3	9.4	0.48	82	37
PreibZinn99-84 …….	K3	145.0	6.0	9.1	2.46	74	31	HD135363	G5(V)	29.4	7.8	6.3	1.14	84	37
HR9 …………	F2IV	39.1	7.3	5.3	3.51	27	31	RE J0723+20	K3(V)	30.0	8.1	7.0	1.09	87	37
PreibZinn99-19 …….	K6	145.0	5.9	8.3	2.6	76	31	GJ803	M1	9.9	7.3	4.8	0.47	30	37
PreibZinn99-68 …….	K2	145.0	6.0	8.0	2.57	83	31	HD 188228	A0V	32.5	7.0	4.0	2.09	89	36
HD172555 …………	A7	29.2	7.3	4.3	3.28	24	31	HD155555C	M4.5	31.4	7.3	7.7	0.51	85	36
BP-Tau …………	K7	140.0	5.8	8.2	2.28	78	30	HD76218	G9-V	26.2	8.7	5.9	1.25	81	36
RX-J1844.3-3541 …..	K5	130.0	6.2	8.6	2.59	77	30	HD25457	F7V	19.2	8.1	4.3	1.33	66	36
HD207129 …………	G2	15.6	7.3	4.3	2.93	14	30	HD105	G0V	40.1	7.5	6.2	1.30	96	35
HR136 …………	A0	45.0	7.3	5.2	3.62	35	30	HD25300	K0	30.0	8.2	6.9	0.97	88	35

TABLE 21

YOUNG STARS WITH HIGHEST PROBABILITY OF PLANET DETECTION

(1)	(2) Spec. Type	(3) Dist. (pc)	(4) Log (Age) (yr)	(5) H (mag)	(6) Mass (M_{Jup})	(7) SMA (AU)	(8) Score (%)	(9) Star	(10) Spec. Type	(11) Dist. (pc)	(12) Log (Age) (yr)	(13) H (mag)	(14) Mass (M_{Jup})	(15) SMA (AU)	(16) Score (%)
	JWST TFI/NRM 4.4 μm									JWST/MIRI 11.4 μm					
TWA9B	M1	60.0	7.0	9.4	0.40	16	49	GJ803	M1	9.9	7.3	4.8	0.51	34	85
PreibZinn99-84	K3	145.0	6.0	9.1	1.29	37	45	GJ3305	M0.5	29.8	7.3	9.4	0.46	49	82
TWA17	K5	60.0	7.0	9.2	1.08	17	45	HD164249	F5	23.7	7.3	6.0	1.23	54	82
GI-Tau	K7	140.0	6.3	9.4	1.34	36	45	HD155555C	M4.5	31.4	7.3	7.7	0.46	51	76
PreibZinn99-11	K7:	145.0	5.9	8.5	1.12	40	45	HD207129	G2	15.6	7.3	4.3	1.37	54	75
TYC7349-2191-1	K2-IV	130.0	6.0	8.4	1.16	35	45	HIP23309	M0/1	26.3	7.3	6.4	0.53	52	72
GSC8862-0019	K4V	60.0	7.5	9.0	0.92	16	44	CD-64d1208	K7	29.2	7.3	6.3	1.32	53	71
TWA18	M0.5	60.0	7.0	9.1	0.45	18	44	AOMen	K6	38.5	7.3	7.0	1.43	59	71
HD285751/v1200-Tau	K2(V)	82.0	6.8	8.9	0.87	23	43	HIP1993	K7	45.0	7.3	7.9	1.42	55	69
TWA12	M2	60.0	7.0	8.3	0.43	16	43	HD37572	K0V	23.9	7.8	5.9	1.54	58	69
PreibZinn99-33	M1	145.0	5.9	9.1	0.52	35	43	2RE-J0255+474	K5Ve	33.0	7.9	7.3	1.58	57	68
RX-J1844.3-3541	K5	130.0	6.2	8.6	1.15	32	43	PPM366328	K0	45.0	7.3	7.7	1.24	65	68
PreibZinn99-69	K5	145.0	6.3	8.8	1.18	37	42	HD17925	K1V	10.4	7.9	4.2	1.34	42	67
PreibZinn99-27	M3	145.0	5.7	9.0	0.50	38	42	QT-AND	G0?	39.0	7.8	7.5	1.60	61	66
PreibZinn99-67	K5	145.0	6.0	8.7	1.18	35	42	HD 172555	A5 IV/V	29.2	7.1	4.3	2.16	56	66
TWA9A	K5	60.0	7.0	8.0	0.87	16	42	HD987	G6	43.7	7.3	7.1	1.48	65	65
V830-Tau	K7	140.0	6.3	8.6	1.11	37	42	RE-J0723+20	K3(V)	30.0	8.1	7.0	1.55	67	64
1RXS-J043243.2-152003	G4V	117.0	6.6	8.7	1.14	32	42	HD35850	F7	26.8	7.1	5.1	1.66	57	64
PreibZinn99-70	M1	145.0	5.7	9.1	0.52	39	42	HD 39060	A5V	19.3	7.3	3.5	2.27	61	64
V836Tau	K7	140.0	6.3	9.1	1.38	35	42	HD200798	A5	45.0	7.3	6.1	2.32	57	64
TWA10	M2.5	60.0	7.0	8.5	0.47	16	42	TWA9A	K5	60.0	7.0	8.0	1.45	60	64
PreibZinn99-59	M0	145.0	6.3	9.2	0.55	35	41	TWA17	K5	60.0	7.0	9.2	1.42	60	63
TWA13	M1	60.0	7.0	7.7	0.48	16	41	TWA6	K7	60.0	7.0	8.2	1.41	69	63
HIP1993	K7	45.0	7.3	7.9	0.98	12	41	BetaPic	A3V	19.3	7.3	3.5	1.99	70	62
RECX10	M0	100.0	6.9	8.9	0.57	26	41	TWA19B	K7	60.0	7.0	8.5	1.59	64	61

TABLE 22

M STARS WITH HIGHEST PROBABILITY OF PLANET DETECTION

(1)	(2) Spec Type	(3) Dist (pc)	(4) Log (Age) (yr)	(5) H (mag)	(6) Mass $M_{\rm Jup}$	(7) SMA (AU)	(8) Score (%)	(9) Star	(10) Spec. Type	(11) Dist. (pc)	(12) Log (Age) (yr)	(13) H (mag)	(14) Mass $M_{\rm Jup}$	(15) SMA (AU)	(16) Score (%)
	JWSTTFI/NRM 4.4 μm								JWST/MIRI 11.4 μm						
TWA9B	M1	60.0	7.0	9.4	0.40	16	49	GJ803	M1	9.9	7.3	4.8	0.51	34	85
PreibZinn99-84	K3	145.0	6.0	9.1	1.29	37	45	GJ3305	M0.5	29.8	7.3	9.4	0.46	49	82
TWA17	K5	60.0	7.0	9.2	1.08	17	45	HD164249	F5	23.7	7.3	6.0	1.23	54	82
GI-Tau	K7	140.0	6.3	9.4	1.34	36	45	HD155555C	M4.5	31.4	7.3	7.7	0.46	51	76
PreibZinn99-11	K7:	145.0	5.9	8.5	1.12	40	45	HD207129	G2	15.6	7.3	4.3	1.37	54	75
TYC7349-2191-1	K2-IV	130.0	6.0	8.4	1.16	35	45	HIP23309	M0/1	26.3	7.3	6.4	0.53	52	72
GSC8862-0019	K4V	60.0	7.5	9.0	0.92	16	44	CD-64d1208	K7	29.2	7.3	6.3	1.32	53	71
TWA18	M0.5	60.0	7.0	9.1	0.45	18	44	AOMen	K6	38.5	7.3	7.0	1.43	59	71
HD285751/v1200-Tau	K2(V)	82.0	6.8	8.9	0.87	23	43	HIP1993	K7	45.0	7.3	7.9	1.42	55	69
TWA12	M2	60.0	7.0	8.3	0.43	16	43	HD37572	K0V	23.9	7.8	5.9	1.54	58	69
PreibZinn99-33	M1	145.0	5.9	9.1	0.52	35	43	2RE-J0255+474	K5Ve	33.0	7.9	7.3	1.58	57	68
RX-J1844.3-3541	K5	130.0	6.2	8.6	1.15	32	43	PPM366328	K0	45.0	7.3	7.7	1.24	65	68
PreibZinn99-69	K5	145.0	6.3	8.8	1.18	37	42	HD17925	K1V	10.4	7.9	4.2	1.34	42	67
PreibZinn99-27	M3	145.0	5.7	9.0	0.50	38	42	QT-AND	G0?	39.0	7.8	7.5	1.60	61	66
PreibZinn99-67	K5	145.0	6.0	8.7	1.18	35	42	HD 172555	A5 IV/V	29.2	7.1	4.3	2.16	56	66
TWA9A	K5	60.0	7.0	8.0	0.87	16	42	HD987	G6	43.7	7.3	7.1	1.48	65	65
V830-Tau	K7	140.0	6.3	8.6	1.11	37	42	RE-J0723+20	K3(V)	30.0	8.1	7.0	1.55	67	64
1RXS-J043243.2-152003	G4V	117.0	6.6	8.7	1.14	32	42	HD35850	F7	26.8	7.1	5.1	1.66	57	64
PreibZinn99-70	M1	145.0	5.7	9.1	0.52	39	42	HD 39060	A5V	19.3	7.3	3.5	2.27	61	64
V836Tau	K7	140.0	6.3	9.1	1.38	35	42	HD200798	A5	45.0	7.3	6.1	2.32	57	64
TWA10	M2.5	60.0	7.0	8.5	0.47	16	42	TWA9A	K5	60.0	7.0	8.0	1.45	60	64
PreibZinn99-59	M0	145.0	6.3	9.2	0.55	35	41	TWA17	K5	60.0	7.0	9.2	1.42	60	63
TWA13	M1	60.0	7.0	7.7	0.48	16	41	TWA6	K7	60.0	7.0	8.2	1.41	69	63
HIP1993	K7	45.0	7.3	7.9	0.98	12	41	BetaPic	A3V	19.3	7.3	3.5	1.99	70	62
RECX10	M0	100.0	6.9	8.9	0.57	26	41	TWA19B	K7	60.0	7.0	8.5	1.59	64	61

TABLE 23

M Stars With Highest Probability of Planet Detection

(1) Star	(2) Spec. Type	(3) Dist. (pc)	(4) Log(Age) (yr)	(5) H (mag)	(6) Mass $M_{\rm Jup}$	(7) SMA (AU)	(8) Score (%)	(9) Star	(10) Spec Type	(11) Dist. (pc)	(12) Log(Age) (yr)	(13) H (mag)	(14) Mass $M_{\rm Jup}$	(15) SMA (AU)	(16) Score (%)
		JWST MIRI 11.4 μm								TMT 1.65 μm					
GJ 206	M3.5	12.8	7.9	6.9	0.46	39	93	GJ 103	M0 VP	11.5	6.4	5.1	0.54	15	63
GJ 494	M0.5	11.4	7.3	5.8	0.42	36	93	GJ 799	M4.5	10.2	7.3	5.2	0.80	16	40
GJ 1284	M3	14.8	7.7	6.6	0.44	45	92	GJ 803	M1	9.9	7.3	4.8	0.85	14	39
GJ 82	M4	12	8.0	7.2	0.46	38	92	GJ 494	M0.5	11.4	7.3	5.8	0.86	15	37
GJ 9520	M1.5	11.4	7.7	6.0	0.47	37	91	GJ 735	M3	11.6	7.4	5.7	1.02	17	33
GJ 103	M0 VP	11.5	6.4	5.1	0.45	39	91	GJ 643	M3.5	6.5	7.6	7.1	0.92	10	29
GJ 277B	M3.5	11.5	7.7	7.0	0.44	36	91	GJ 1284	M3	14.8	7.7	6.6	1.23	18	26
GJ 875.1	M3	14.2	7.8	7.1	0.46	40	91	GJ 644A	M2 V	5.7	7.7	4.8	1.01	8	26
GJ 277A	M2.5	11.4	7.7	6.2	0.44	34	91	GJ 277B	M3.5	11.5	7.7	7.0	1.07	16	25
GJ 781.1A	M3.0	14.6	8.2	7.7	0.44	42	90	GJ 277A	M2.5	11.4	7.7	6.2	1.13	15	25
GJ 735	M3	11.6	7.4	5.7	0.44	37	88	GJ 9520	M1.5	11.4	7.7	6.0	1.10	16	24
GJ 431	M3.5	10.5	8.0	6.8	0.44	36	88	GJ 875.1	M3	14.2	7.8	7.1	1.35	19	21
GJ 643	M3.5	6.5	7.6	7.1	0.47	26	86	GJ 206	M3.5	12.8	7.9	6.9	1.40	15	16
GJ 803	M1	9.9	7.3	4.8	0.55	36	85	GJ 82	M4	12.0	8.0	7.2	1.45	15	14
GJ 799	M4.5	10.2	7.3	5.2	0.48	33	84	GJ 431	M3.5	10.5	8.0	6.8	1.48	12	14
GJ 285	M4.5	5.9	8.1	6.0	0.44	23	81	GJ 285	M4.5	5.9	8.1	6.0	1.35	11	13
GJ 644A	M2 V	5.7	7.7	4.8	0.47	24	80	GJ 896A	M3.5	6.3	8.2	5.6	1.39	10	12
GJ 896A	M3.5	6.3	8.2	5.6	0.46	26	80	GJ 4247	M4.5 V	9.0	8.3	7.0	1.75	14	7
GJ 3148A	M3 V	14.3	8.3	7.3	0.51	48	75	GJ 781.1A	M3.0	14.6	8.2	7.7	1.80	17	6
GJ 4247	M4.5 V	9.0	8.3	7.0	0.49	38	70	GJ 3148A	M3 V	14.3	8.3	7.3	1.81	13	4
GJ 208	M0.5 V	11.4	8.4	5.4	0.51	56	58	GJ 208	M0.5 V	11.4	8.4	5.4	1.87	14	3
GJ 487	M3	10.2	8.5	6.3	0.60	47	51	GJ 725A	K5	3.6	9.7	4.7	0.40	0	2
GJ 699	M4	1.8	9.9	4.8	0.49	12	46	GJ 725B	K5	3.5	9.7	5.2	0.43	0	1
GJ 447	M4	3.3	9.5	6.0	0.52	21	45	GJ 729	M3.5	3.0	8.9	5.7	0.34	0	1
GJ 362	M3	11.5	8.5	6.7	0.84	41	42	GJ 411	M2 V	2.6	9.5	3.7	1.40	0	0

REFERENCES

Agol, E. 2007, MNRAS, 374, 1271

Baraffe, I., Chabrier, G., Barman, T. S., Allard, F., & Hauschildt, P. H. 2003, A&A, 402, 701

Baudoz, P., Boccaletti, A., Riaud, P., Cavarroc, C., Baudrand, J., Reess, J. M., & Rouan, D. 2006, PASP, 118, 765

Beckwith, S. 2009, ApJ, 684, 1404

Beichman, C. A. 2001 in ASP Conf. Ser. 244, Young Stars Near Earth: Progress and Prospects, ed. R. Jayawardhana, & T. Greene (San Francisco: ASP), 376

Bennett, D. P., Anderson, J., & Gaudi, B. S. 2007, ApJ, 660, 781

Beuzit, J.-L., et al. 2006, Messenger, 125, 29

Biller, B. A., et al. 2007, ApJS, 173, 143

Biller, B., et al. 2009, AIP Conf. Ser., 1094, 425

Boccaletti, A., Carbillet, M., Fusco, T., Mouillet, D., Langlois, M., Moutou, C., & Dohlen, K. 2008, in Proc. SPIE 7015, Adaptive Optics Systems, ed. N. Hubin, C. E. Max, & P. L. Wizinowich, 70156E

Boccaletti, A., Riaud, P., Baudoz, P., Baudrand, J., Rouan, D., Gratadour, D., Lacombe, F., & Lagrange, A.-M. 2004, PASP, 116, 1061

Boccaletti, A., Baudoz, P., Baudrand, J., Reess, J. M., & Rouan, D. 2005, Adv. Space Res., 36, 1099

Boss, A. 2000, ApJ, 545, L61

Brown, R. A. 2009, ApJ, 702, 1237

Burrows, A., Sudarsky, D., & Lunine, J. I. 2003, ApJ, 596, 587

Butler, R. P., Johnson, J. A., Marcy, G. W., Wright, J. T., Vogt, S. S., & Fischer, D. A. 2006, PASP, 118, 1685

Chauvin, G., et al. 2005, A&A, 438, L29

Chiang, E., Kite, E., Kalas, P., Graham, J. R., & Clampin, M. 2009, ApJ, 693, 734

Cumming, A. 2004, MNRAS, 354, 1165

Cumming, A., Butler, R. P., Marcy, G. W., Vogt, S. S., Wright, J. T., & Fischer, D. A. 2008, PASP, 120, 531

Deming, D., et al. 2009, preprint (arXiv:0903.4880)

Dodson-Robinson, S. 2008, Ph.D. thesis, Univ. California (Santa Cruz)

Dodson-Robinson, S., Ford, E., Beichman, C. A., & Veras, D. 2009, ApJ, 707, 79

Doyon, R., et al. 2008, in Proc. SPIE 7010, Space Telescopes and Instrumentation 2008: Optical, Infrared, and Millimeter, ed. J. M. Oschmann, Jr., M. W. M. de Graauw, & H. A. MacEwen, 70100X

Eiroa, C., et al. 2002, A&A, 384, 1038

Elias, J. 1978, ApJ, 224, 857

Encrenaz, T. 1999, Astron. Astrophys. Rev., 9, 171

Evans, J. J., III, et al. 2003, PASP, 115, 965

Fortney, J., et al. 2008, ApJ, 683, 1104

Gardner, J., et al. 2006, Space Sci. Rev., 123, 485

Golimowski, D. A., Durrance, S. T., & Clampin, M. 1993, ApJ, 411, L41

Gould, A., & Loeb, A. 1992, ApJ, 396, 110

Green, J. J., et al. 2005, Proc. SPIE 5905, Techniques and Instrumentation for Detection of Exoplanets II, ed. D. R. Coulter, 185

Greene, T., & Beichman, C., et al. 2007, Proc. SPIE 6693, Techniques and Instrumentation for Detection of Exoplanets III, ed. D. R. Coulter

Heinze, A. N., Hinz, P. M., Kenworthy, M., Miller, D., & Sivanandam, S. 2008, ApJ, 688, 583

Helled, R., & Schubert, G. 2009, ApJ, 697, 1256

Hillenbrand, et al. 2008, ApJ, 677, 630

Huélamo, N., et al. 2008, A&A, 489, 9

Hinkley Sasha Oppenheimer, B. R., Brenner, D., Parry, I. R., Sivaramakrishnan, A., Soummer, R., & King, D. 2008 in Proc. SPIE 7015, Adaptive Optics Systems, ed. N. M. Hubin, C. E. Wizinowich, & L. Peter, 701519

Ida, S., & Lin, D. N. C. 2005, ApJ, 626, 1045

Kohnson, J. A. 2008, in ASP Conf. Ser. 398, Extreme Solar Systems, ed. D. Fischer, F. A. Rasio, S. E. Thorsett, & A. Wolszczan, 59

Johnson, J. A., Butler, R. P., Marcy, G. W., Fischer, D. A., Vogt, S. S., Wright, J. T., & Peek, K. M. G. 2007, ApJ, 670, 833

Kalas, P., et al. 2008, Science, 322, 1345

Kenworthy, et al. 2009, ApJ, 697, 1928

Krist, J. 2007, in In the Spirit of Bernard Lyot: The Direct Detection of Planets and Circumstellar Disks in the 21st Century, ed. P. Kalas (Berkeley: Univ. California)

Kuchner, M., & Traub, W. A. 2002, ApJ, 570, 900

Lafrenière, et al. 2007, ApJ, 670, 1367

Lagrange, A. M., et al. 2009, A&A, 493, L21

Lloyd, J., et al. 2006, ApJ, 650, L131

Lovis, C., Mayor, M., Bouchy, F., Pepe, F., Queloz, D., Udry, S., Benz, W., & Mordasini, C. 2009, in IAU Symp. 253, Transiting Planets, Proc. IAU, 502

Macintosh, B., et al. 2006, in Proc. SPIE 6272, Advances in Adaptive Optics II, ed. B. L. Ellerbroek, & D. Bonaccini Calia, 62720L

Macintosh, B., & GPI Consortium 2007, In the Spirit of Bernard Lyot: The Direct Detection of Planets and Circumstellar Disks in the 21st Century, ed. P. Kalas (Berkeley: Univ. California)

Makarov, V. V., Beichman, C. A., Catanzarite, J. H., Fischer, D. A., Lebreton, J., Malbet, F., & Shao, M. 2009, ApJ, 707, 73

Marley, M. S., Fortney, J. J., Hubickyj, O., Bodenheimer, P., & Lissauer, J. J. 2007, ApJ, 655, 541

Marois, C., et al. 2008, Science, 322, 1348

Martin, E. L., Dahm, S., & Pavlenko, Y. 2001, Astrophysical Ages Times Scales, 245, 349

Metchev, S. A., & Hillenbrand, L. A. 2009, ApJS, 181, 62

McCarthy, C., & Zuckerman, B. 2001, AJ, 127, 2871

Meyer, M. R., et al. 2006, PASP, 118, 1690

Neuhäuser, R., Guenther, E. W., Wuchterl, G., Mugrauer, M., Bedalov, A., & Hauschildt, P. H. 2005, A&A, 435, L13

Oppenheimer, B., & Hinckley, S. 2009, Ann. Rev. Astron. Astrophys., 47, 253

Oppenheimer, B. R., Golimowski, D. A., Kulkarni, S. R., Matthews, K., Nakajima, T., Creech-Eakman, M., & Durrance, S. T. 2001, AJ, 121, 2189

Pan, X., Shao, M., & Kulkarni, S. R. 2004, Nature, 427, 326

Plavchan, P., Werner, M. W., Chen, C. H., Stapelfeldt, K. R., Su, K. Y. L., Stauffer, J. R., & Song, I. 2009, ApJ, 698, 1068

Pollack, J. B., Hubickyj, O., Bodenheimer, P., Lissauer, J. J., & Podolak, M. 1996, Icarus, 124, 62

Pott, J.-U., et al. 2008, in Astrometry and Imaging with the Very Large Telescope Interferometer, preprint arXiv0811.2264P
Prato, L., Huerta, M., Johns-Krull, C. M., Mahmud, N., Jaffe, D. T., & Hartigan, P. 2008, ApJ, 687, L103
Preibisch, T., & Feigelson, E. D. 2005, ApJS, 160, 390
Preibisch, T., & Zinnecker, H. 1999, AJ, 117, 2381
Rieke, G. R., et al. 2005, ApJ, 620, 1010
Rieke, M., Kelly, D., & Horner, S. 2005, Proc. SPIE, 5904, 590401
Rouan, D., Boccaletti, A., Baudoz, P., Cavarroc, C., Baudrand, J., & Reess, J. M. 2007, in In the Spirit of Bernard Lyot: The Direct Detection of Planets and Circumstellar Disks in the 21st Century, ed. P. Kalas (Berkeley: Univ. California)
Saumon, D., Hubbard, W. B., Burrows, A., Guillot, T., Lunine, J. I., & Chabrier, G. 1996, ApJ, 460, 993
Schneider, J. 2009, Exoplanet Encyclopedia, http://exoplanet.eu
Setiawan, J., Henning, Th., Launhardt, R., Müller, A., Weise, P., & Küster, M. 2008, Nature, 451, 38
Siess, L., Dufour, E., & Forestini, M. 2000, A&A, 358, 593
Sivaramakrishnan, A., Tuthill, P., Ireland, M., Lloyd, J., Martinashe, F., Soummer, R., Makidon, R., Doyon, R., Beaulieu, M., & Beichman, C. A. 2009, Proc. SPIE, 7440, 74400Y
Sivaramakrishnan, A., Soummer, R., Pueyo, L., Wallace, J. K., & Shao, M. 2008, ApJ, 688, 701
Suzuki, R., et al. 2009, American Institute of Physics Conference Series, 1158, 293
Sousa, S. G., Santos, N. C., & Mayor, M., et al. 2009, in AIP Conf. Proc. 1094, Cool Stars, Stellar Systems and The Sun: Proc. 15th Cambridge Workshop on Cool Stars, Stellar Systems and the Sun, 477
Sozzetti, A., et al. 2008 in Proc. IAU Symp. 248, A Giant Step: From Milli- to Micro-arcsecond Astrometry, ed. W. J. Jin, I. Platais, & M. A. C. Perryman, 256
Stahl, H. P. 2007, Proc. SPIE, 6671, 667102
Tanner, A., et al. 2007, PASP, 119, 747
Tannirkulam, A., et al. 2008, ApJ, 689, 513
Torres, C. A. O., Quast, G. R, Melo, C. H. F, & Sterzik, M. F. 2008, in Handbook of Star Forming Regions: Vol. II, ed. B. Reipurth (San Francisco: ASP) 757
Traub, W. A., et al. 2009, preprint arXiv:0904.0822
Trauger, J. A., & Traub, W. A. 2007, Nature, 446, 771
Unwin, S. R., et al. 2008, PASP, 120, 38
Unwin, S. C., Catanzarite, J., & Shao, M. 2009, American Astronomical Society, DDA meeting #40, #17.05
Van Belle, G., et al. 2008, Messenger, 134, 6
Valenti, J. A., & Fischer, D. A. 2005, ApJS, 159, 141
Veras, D., Crepp, J. R., & Ford, E. B. 2009, ApJ, 696, 1600
Wahhaj, Z., et al. 2009, AAS Meeting Abstracts, 214, #300.04
Wilking, B. A., Gagné, M., & Allen, L. E. 2008, in Handbook of Star Forming Regions, Volume II: The Southern Sky, ed. B. Reipurth, (San Francisco: ASP) 351
Zapatero Osorio, M. R., Martín, E. L., Béjar, V. J. S., Bouy, H., Deshpande, R., & Wainscoat, R. J. 2007, ApJ, 666, 1205
Zimmerman, N., et al. 2009, ApJ, 709, 733
Zuckerman, B., & Song, I. 2004, ARAA, 42, 685